Materials Advances

ROYAL SOCIETY OF CHEMISTRY

PAPER

View Article Online
View Journal | View Issue

Check for updates

Cite this: *Mater. Adv.*, 2025, 6, 8615

Unveiling phase dependent physical properties of cubic and hexagonal $CsCdBr_3$: a DFT approach

Arpon Chakraborty, *[a] M. N. H. Liton, [b] Mst. Halima Khatun[a] and Md. Shahjahan[a]

Received 29th June 2025,
Accepted 7th October 2025

DOI: 10.1039/d5ma00693g

rsc.li/materials-advances

The distinctive structural, optoelectronic, photocatalytic, and elastic properties of $CsCdBr_3$ make it appropriate for cutting-edge technological applications. Important ground-state properties of the cubic and hexagonal phases of $CsCdBr_3$ are investigated in this work using density functional theory (DFT). Both phases are energetically and mechanically stable. Electronic band structure analysis revealed that both $CsCdBr_3$ polymorphs exhibit semiconducting character. The cubic phase shows an indirect bandgap (2.74 eV) while the hexagonal phase possesses a direct bandgap (4.26 eV). The density of states (DOS), Mulliken bond, and charge density distribution provide orbital contributions to the band structure and bonding nature of the polymorphs. The calculated redox potential suggested that both compounds are capable of water splitting as well as breaking down biological contaminants under UV-vis radiation. By analyzing the different elastic parameters, it can be concluded that both polymorphs are soft and ductile in nature. The cubic phase exhibits better transport properties, while the hexagonal phase showcases a degree of anisotropy in thermal properties. The optical characteristics correspond well with the electronic band structure. The high absorptivity in the UV region, lower reflectivity, and optical anisotropy of the hexagonal polymorph suggested that these could be a potential candidate for applications in the photovoltaic solar industry as well as to design waveguides, dielectric condensers, light emitting diodes (LEDs), and thermoelectric and sensing devices.

1. Introduction

The rapid population growth and mismanagement of waste materials due to this huge population have contaminated our environment. Traditional purifiers cannot cope with this increase in pollutants. In addition to this, population growth has created a global energy crisis, driving urgent demand for sustainable, efficient, and environmentally friendly energy solutions. In this context, semiconductor-based photocatalysts are widely utilized to degrade organic pollutants, decrease CO_2, and split water into hydrogen and oxygen using solar energy. As a result, photocatalysis is regarded as a feasible method for reducing pollution and alleviating the energy problem, and it has received significant attention in recent years. The principal drawbacks of photocatalytic CO_2 reduction are exacerbated by low energy conversion efficiencies and a lack of suitable catalysts. However, for water splitting for hydrogen production, wastewater treatment, and pollutant degradation, some requirements, such as the ideal bandgap, proper conduction band minima (CBM), valence band maxima (VBM), and a lower electron–hole recombination rate, must be satisfied. Semiconducting compounds such as WO_3,[1,2] ZnO,[3,4] Fe_2O_3,[5] Ta_2O_5,[6] $BiVO_4$,[7–9] $RbSr_2Nb_3O_{10}$,[10] $BaTiO_3$,[11] $BaTi_2O_5$,[12] and $CsNbO_3$[13] are used widely as photocatalysts. However, the photocatalytic performance of these compounds is still not up to the mark, and as a result, researchers are trying to find new photocatalysts with higher efficiency. Thermoelectric (TE) materials are solid-state semiconductors that can convert thermal energy into electricity, and *vice versa*, exploiting the Seebeck (S) and Thomson effects. They are good for the environment as well as provide interesting benefits for a variety of scientific applications.[14,15] TE materials are extensively used to convert waste heat from automobiles, boilers and furnaces, jet engines, *etc.* into electricity, using cooling or heating processes. There are a large number of materials including perovskites, double perovskites, chalcogenides and oxy-chalcogenides that have high potential for use in thermal applications.[11,15–19] However, most of these materials have a very low value of S resulting in limited applications. An alternative application of these materials has emerged in the cooling process if they possess a high power density ($S^2\sigma$) and have a compact form factor.

In recent decades, much effort has been devoted to the study of oxide perovskites with the general chemical formula AMO_3. For halide equivalents, however, not much study has been

---

[a] *Department of Physics, Gopalganj Science and Technology University, Gopalganj-8105, Bangladesh. E-mail: iamarpon07@gmail.com*
[b] *Department of Physics, Begum Rokeya University, Rangpur-5403, Bangladesh*

done. Perovskites and double perovskites have inherent qualities that are desirable. Due to their possible applications for use in solar cells, photocatalysis, light-emitting diodes, and electronic devices, they have become an important area of study for the research communities.[20–28] Due to their three-dimensional corner sharing network of octahedra, perovskite structures represent a highly tunable class of materials with impressive carrier mobility and wide energy bandgaps.[29–31] Replacement of halogens with various species may alter energy gaps and electronic transport properties depending on their symmetry. One member of this family, cesium cadmium tribromide ($CsCdBr_3$), has interesting structural polymorphism with distinct hexagonal ($P6_3/mmc$) and cubic ($Pm\bar{3}m$) phases that can be controlled by synthesis conditions and have notably different physical properties. The cubic phase is similar to typical perovskites like $CsPbBr_3$.[32] The hexagonal phase, on the other hand, has a distinct one-dimensional chain-like arrangement of $[CdBr_6]^{4-}$ octahedra,[33] which results in exceptional electrical and mechanical properties.

Cd-based thermoelectrics are promising for high-temperature, controlled environments (*e.g.*, aerospace, industrial waste heat recovery) where toxicity risks are manageable, unlike consumer electronics. Their high ZT justifies exploration in such contexts, especially with mitigation strategies. In addition, Cd-based compounds have remarkable photovoltaic and optoelectronic applications. Though Cd toxicity is a concern (*e.g.*, bioaccumulation), in perovskites, it is less bioavailable than elemental Cd. Applications like PV/TE require encapsulation to mitigate risks, similar to CdTe solar cells. This highlights the need for careful lifecycle management and recycling protocols if these materials are to be developed further. It also motivates future computational studies to explore less toxic alternatives (*e.g.*, substituting Cd with Zn, Sn, or Ge) while aiming to retain the desirable properties identified here. There are a few compounds, namely, Cs_2CdBr_4 and Cs_3CdBr_5, which have the same materials but have different structures. Moreover, these compounds have less favorable band alignments for photocatalytic and photovoltaic applications, making them less promising than $CsCdBr_3$.

Although $CsCdBr_3$ is technologically relevant, the ground state physical characteristics of cubic and hexagonal $CsCdBr_3$ have not been systematically compared theoretically and experimentally. Both $CsCdBr_3$ polymorphs have been synthesized and characterized by several research groups since the 1970s, although Natta *et al.*[34] reported the existence of cubic $CsCdBr_3$ back in 1928. Møller *et al.*[35] reported the hexagonal phase of $CsCdBr_3$ in 1977. Later studies on cubic $CsCdBr_3$ often emphasize its optical properties or doping,[36–40] suggesting that earlier synthesis methods were established.

Polymorphism is a common phenomenon in perovskite materials and has an enormous effect on how they are applied. From corner-sharing to face-sharing octahedral connectivity, the cubic-to-hexagonal transition in perovskites demands significant structural rearrangement. Hayashi *et al.*[41] studied this change in oxide perovskites, including $SrFeO_3$, and found that maintaining the hexagonal structure depends critically on the electronic configuration of the B-site cation. As reported by Rao and Rao,[42] similar changes to halide systems have been observed in $CsCdCl_3$ and $CsCdI_3$, suggesting a general characteristic of cesium cadmium halides. Wenzel *et al.*[43] experimentally studied the band structure of $CsCdBr_3$. They discovered that the conduction band is divided into two parts: a lower, isolated, and very narrow band and higher lying ones. The presence of localized excitons at lattice defects further enhances the material's luminescence properties. Vtyurina *et al.*[36] studied a Bi-doped cubic $CsCdBr_3$ structure and found that it exhibits photoluminescence in the near-IR range due to point defects, making it a potential luminescent material. Perfect-blue emission with higher photoluminescence results from Pb^{2+} doping in $CsCdBr_3$ nanorods, which is applicable for light-emitting diode (LED) uses, as reported by Guo *et al.*[37] S. Berri and N. Bouarissa[24] studied the electronic and optical properties of the cubic $CsCdBr_3$. They confirmed the existence of an indirect bandgap. Though there exist some other phases like Cs_2CdBr_4 and Cs_3CdBr_5, those have different crystallographic structures (*e.g.*, 2D layered or isolated polyhedra) leading to fundamentally different electronic, optical, and transport properties.

From the literature review on halide perovskites, several knowledge gaps remain in our understanding of $CsCdBr_3$. The structural, electronic, optical, photocatalytic, thermal and mechanical properties of cubic and hexagonal $CsCdBr_3$ have not yet been systematically compared in any previous study. The influence of structural differences on the electronic and optical properties, particularly the nature of the bandgap and optical absorption spectra, remains unclear. The elastic stability of the two polymorphs, which is critical for their practical applications, has not been comprehensively characterized. Based on the aforementioned discussion, the present study focuses on $CsCdBr_3$ polymorphs due to their unique structural stability, optoelectronic properties, photocatalytic properties, thermoelectric properties, *etc.*, using first principles calculations. Moreover, $CsCdBr_3$ polymorphs are understudied compared to other halide perovskites. This study will also help suggest suitable areas of photovoltaic, photocatalytic and thermoelectric applications as well as act as a guide for future experimental studies.

2. Computational details

In this study, we used the CAmbridge Serial Total Energy Package (CASTEP) code[44] based on density functional theory (DFT) to investigate all the properties except the thermoelectric properties. The Perdew–Burke–Ernzerhof (PBE) functional[45] in the generalized gradient approximation (GGA) was chosen for exchange correlations. Properties like structural relaxation, elastic properties, and optical properties were evaluated using this functional. Moreover, for electronic property calculations, the Heyd–Scuseria–Ernzerhof (HSE06) functional was used.[46] For the interactions of charges between the atomic core and valence electrons, the ultrasoft pseudopotential of Vanderbilt-type was employed.[47] The plane-wave cut-off energy was set to 400 eV and 460 eV for the cubic and hexagonal phases, respectively, whereas the k-point for the Brillouin zone (BZ) was sampled using $18 \times 18 \times 18$ and $8 \times 8 \times 8$ Monkhorst–Pack grid schemes[48] for the respective phases. The valence electron configurations for Cs, Cd, and Br are [$4d^{10}5p^{6}6s^{1}$], [$4p^{6}4d^{10}5s^{2}$], and [$4s^{2}3d^{10}4p^{5}$], respectively. The Broyden–Fletcher–Goldfarb–Shanno (BFGS) minimization algorithm[49] was used to optimize the equilibrium structure. During the geometry optimization process, a total energy convergence tolerance of 1×10^{-6} eV per atom, a maximum interatomic force of 0.03 eV Å^{-1}, a maximum stress of 0.05 GPa, and a maximum ionic displacement of 1×10^{-3} Å were set. The independent elastic constants, bulk modulus, and shear modulus were calculated using the stress–strain method existing in the CASTEP code.

Optical properties were obtained by evaluating the complex dielectric function within the independent-particle approximation (IPA), as implemented in CASTEP.[50] The complex dielectric function is written as $\varepsilon(\omega) = \varepsilon_1(\omega) + i\varepsilon_2(\omega)$, where $\varepsilon_1(\omega)$ and $\varepsilon_2(\omega)$ are known as the real and imaginary parts of the dielectric constants, respectively. The electrical band structure is used to determine the imaginary portion, $\varepsilon_2(\omega)$, using the following formula:[51,52]

$$\varepsilon_2(\omega) = \frac{2e^2\pi}{\Omega\varepsilon_0}\sum_{k,v,c} K\left|\left\langle \Psi_k^c \middle| \hat{u}\cdot\hat{r} \middle| \Psi_k^v \right\rangle\right|^2 \delta\left(E_k^c - E_k^v - E\right)$$

In this equation, Ω is the volume of the unit cell, ω is the angular frequency of the electromagnetic wave, e is the electronic charge, and Ψ_k^c and Ψ_k^v are the conduction and valence band wave functions at a given wave vector k, respectively. The well-known Kramers–Kronig relationships can be used to derive the real part $\varepsilon_1(\omega)$ of the dielectric function from the imaginary part $\varepsilon_2(\omega)$:[53]

$$\varepsilon_1(\omega) = 1 + \frac{2}{\pi}P\int_0^\infty \frac{\omega'\varepsilon_2(\omega')}{\omega'^2 - \omega^2}\mathrm{d}\omega'$$

where P signifies the principal value of the integral.

From the above equations of the real and imaginary dielectric constants, the additional optical parameters such as the absorption coefficient, refractive index, reflectivity, photoconductivity, and energy loss function can be calculated using standard relations.[54,55]

Furthermore, semiclassical Boltzmann theory in which scattering time is taken as a constant, as implemented in the BoltzTraP2[56] code interfaced with Vienna ab initio simulation package (VASP)[57,58] using constant relaxation time approximation (CRTA), was used to predict thermoelectric transport properties based on input data obtained from CASTEP calculations. Phonon dispersion spectra were calculated using phonopy[59,60] with the VASP interface, wherein the density functional perturbation theory (DFPT) method was used. Moreover, *ab initio* molecular dynamics (AIMD) simulations were performed using the Forcite tools. The NPT thermodynamic ensemble was designated to assess the thermal stability of the polymorphs under investigation at room temperature (298 K).

3. Results and discussion

3.1 Structural properties

$CsCdBr_3$ exhibits polymorphism, crystallizing in both cubic (space group $Pm\bar{3}m$) and hexagonal (space group $P6_3/mmc$) structures. The fundamental variations in these structures provide distinct physical properties that necessitate careful knowledge of their crystallography. The cubic polymorph of $CsCdBr_3$ has the classic ABX_3 perovskite structure with perfect corner-sharing octahedra, as shown in Fig. 1(a). Cd^{2+} ions occupy the center of the unit cell (B-site), surrounded by six Br^- ions forming regular $CdBr_6$ octahedra. Cs^+ ions are positioned at the cube corners (A-site), with a 12-fold coordination environment. Each Cs^+ ion is bonded to 12 equivalent adjacent Br^- atoms, forming a $CsBr_{12}$ cuboctahedron. The Cd–Br–Cd bond angles are 180°, which is characteristic of ideal perovskites. The Cd–Br bond lengths are all equivalent and calculated to be 2.813 Å (Table 4). The Goldschmidt tolerance factor (t) can be used to predict the formability of metal halide perovskites. It is calculated using the formula:

$$t = \frac{r_1 + r_3}{\sqrt{2}(r_2 + r_3)}$$

where r_1, r_2, and r_3 are the ionic radii of A, B, and X ions, respectively. It is approximately 0.87, which falls within the range typically associated with stable cubic perovskites ($0.8 < t < 1.0$).[61]

The hexagonal polymorph of $CsCdBr_3$, on the other hand, deviates significantly from the cubic structure, adopting a

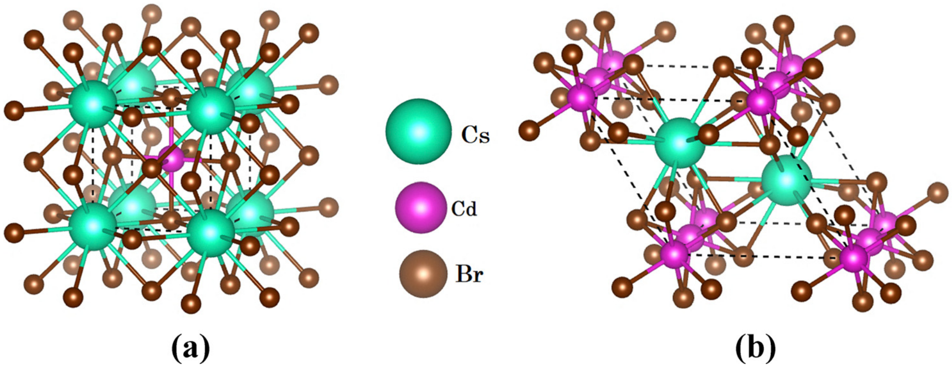

Fig. 1 Schematic 3D crystal structure of the (a) cubic and (b) hexagonal phases of $CsCdBr_3$.

distinctive one-dimensional chain-like arrangement as shown in Fig. 1(b). The structure is composed of face-sharing $CdBr_6$ octahedra that form one-dimensional chains along the *c*-axis. Each Cd^{2+} ion is coordinated to six Br^- ions, but the octahedra are slightly distorted. The distortion directions of all octahedra are almost parallel, leading to a buildup of the nonlinear optical coefficient.[62] The Cd–Br bond lengths within each octahedron are equivalent, with bond lengths of 2.825 Å (Table 4). Cs^+ ions are located between the chains in a 9-fold coordination environment.

The optimized lattice parameters of both structures with available experimental data are listed in Table 1. The optimized lattice parameters were found to be larger than the corresponding experimental ones. It is a well-known shortcoming of the GGA-PBE functional, as it tends to overestimate the lattice parameters. The structural stability of the two polymorphs was ensured by calculating their cohesive energy (E_{coh}) using the following relations.[63,64]

$$E_{coh} = -\frac{[E_{tot} - (xE_{Cs} + yE_{Cd} + zE_{Br})]}{x + y + z}$$

where E_{tot} represents the total energy of the unit cell of $CsCdBr_3$, and E_{Cs}, E_{Cd}, and E_{Br} represent the energy values of Cs atoms, Cd atoms, and Br atoms, respectively. x, y, and z represent the corresponding number of Cs, Cd, and Br atoms in the unit cell. The cohesive energy of the cubic and the hexagonal phases was found to be −2.588 and −2.622 eV per atom, respectively. It suggests that both polymorphs are energetically stable because of the negative value of their respective E_{coh}.

Additionally, formation enthalpy is another indication of the stability of a structure. To assess phase stability against decomposition into competing binaries, the formation energy was evaluated relative to CsBr and $CdBr_2$:

$$\Delta H_f \approx \Delta E_f = E_{CsCdBr_3} - (E_{CsBr} + E_{CdBr_2})$$

The formation enthalpy of the cubic and the hexagonal phases was found to be −25.8 and −61.2 meV, respectively. Both polymorphs are thermodynamically stable against decomposition into CsBr + $CdBr_2$. The energy difference is 35.4 meV per atom, which indicates that the hexagonal structure is more stable than the cubic phase at 0 K. Therefore, this amount of thermal energy is required for the phase transition. Similar energy differences are also found for the cubic to hexagonal or hexagonal to cubic phase transitions that occur in various halide perovskite materials reported by Ivan Ornelas-Cruz *et al.*[65] Similar energy differences are observed in $CsPbBr_3$ (between cubic and orthorhombic).[66] Fadla *et al.*[67] found that $CsPbI_3$ is most stable in the orthorhombic phase, while its cubic phase is thermodynamically stable at 583 K.[65] But according to our study, although the cubic $CsCdBr_3$ is less stable than the hexagonal phase, this phase could be stabilized or could exist as a metastable phase under certain conditions (*e.g.*, strain, finite size effects, specific substrates, and high temperatures).

Phonon dispersion spectra provide vital information about the dynamical stability of a compound. The phonon dispersion curves have been calculated along the high symmetry directions of the Brillouin zone, as shown in Fig. 2(a) and (c). Typically, stable phonon structures exhibit real frequencies, whereas unstable structures are characterized by imaginary frequencies. The computed phonon spectra revealed that both the cubic and hexagonal $CsCdBr_3$ polymorphs display a negative phonon frequency (~ -0.45 THz), indicating localized instabilities or particular vibrational modes impacting certain orientations or regions inside the crystal lattice.[70] Several halide perovskites such as $TlPbF_3$, $CsPbBr_3$, $TlCdF_3$, $RbSrF_3$, *etc.* show imaginary phonon frequency, *i.e.*, unstable at 0 K but found stable at high temperatures.[71,72] Yang *et al.*[72] found that the imaginary phonon modes with a negative frequency originated from the permanent displacement of the atoms due to deformation of the crystal lattice.

To evaluate the thermal stability of $CsCdBr_3$ polymorphs, *ab initio* molecular dynamics (AIMD) simulations were performed at room temperature over a period of 10 ps, utilizing a time step of 0.5 fs. Fig. 2(b) and (d) reveal that minimal energy fluctuations occurred over the simulation time period. Both structures retained their original configurations and had no visible structural abnormalities. The structures retained their integrity over the 10 ps simulation, which suggests stability at room temperature on this timescale. This is consistent with the experimentally observed data, because both the polymorphs of $CsCdBr_3$ have been experimentally synthesized and reported in ref. 36, 37 and 62, which inherently confirms its stability.

3.2 Electronic properties

Electronic band structures of the cubic and hexagonal phases of $CsCdBr_3$ are calculated along the high symmetry directions (X–R–M–Γ–R) and (Γ–A–H–K–Γ–M–L–H), respectively, in the

Table 1 Calculated lattice parameters *a*, *b*, and *c* (Å), equilibrium cell volume V_0 (Å^3), cohesive energy E_{coh} (eV per atom), and formation enthalpy ΔH_f (eV per atom) of the $CsCdBr_3$ polymorphs

Compound	Phase	*a*, *b*, *c*	*V*	E_{coh}	ΔH_f	Ref.
$CsCdBr_3$	Cubic	$a = b = c = 5.628$	178.244	−2.588	−0.0258	This work
		$a = b = c = 5.53$	—	—	—	34[a]
		$a = b = c = 5.65$	180.51	—	—	24[b]
		$a = b = c = 5.617$	177.25	−2.571	—	68[b]
	Hexagonal	$a = b = 7.899$, $c = 6.922$	374.091	−2.622	−0.0618	This work
		$a = b = 7.7281$, $c = 6.742$	—	—	—	62[a]
$CsPbBr_3$	Cubic	$a = b = c = 5.988$	214.663	—	−1.26	69[c]
$CsPbI_3$	Cubic	$a = b = c = 6.34$	—	—	3.2×10^{-4}	67

[a] Experimental values. [b] Theoretical values. [c] Formation energy calculated from kJ mol^{-1} to eV per atom.

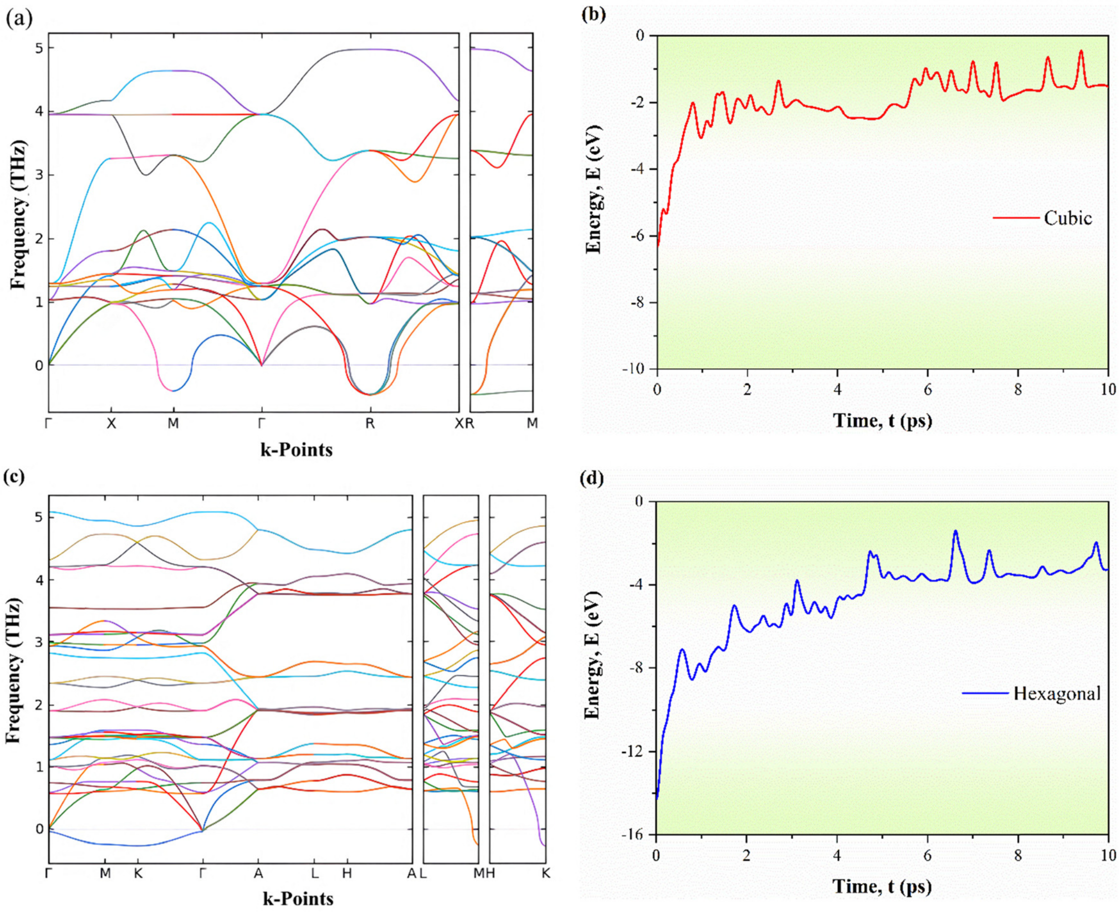

Fig. 2 Phonon dispersion of the (a) cubic and (c) hexagonal phases of $CsCdBr_3$. AIMD simulation of the (b) cubic and (d) hexagonal structures of $CsCdBr_3$.

first Brillouin zone (BZ) at zero pressure and temperature. Both GGA-PBE and HSE06 functionals were used for calculating the band structures, as can be seen in Fig. 3(a)–(d). The horizontal red dashed line indicates the Fermi level, E_F. As per our calculations, the valence band maximum (VBM) for the cubic structure lies on the high-symmetry point R, whereas the VBM lies on the Γ-point for the hexagonal phase. The conduction band minimum (CBM), on the other hand, lies on the Γ-line for both phases. It simply indicates that the cubic phase possesses an indirect bandgap while the hexagonal phase has a direct bandgap. From Table 2, it can be seen that the estimated values of the bandgap using GGA-PBE and HSE06 functionals are 0.637 eV and 2.740 eV, for the cubic phase, while 2.87 eV and 4.26 eV for the hexagonal phase, respectively. The calculated bandgap values for both structures are consistent with the available theoretical[24,67] and experimental[62] results. It is well known that the PBE functional frequently underestimates the bandgap of a semiconductor or an insulator.[73] On the other hand, HSE06 values are expected to provide a more accurate estimate.[46] The cubic $CsCdBr_3$ has a bandgap value within the visible range, while the hexagonal structure has that in the lower-UV range. It makes them appropriate for use in different optoelectronic applications, in contrast to other perovskites like $BaTiO_3$ and $ZnSbF_3$.[11,74]

It is also known that the highly dispersive band indicates higher carrier mobility due to lower carrier effective mass and *vice versa*. From Fig. 3(a)–(d), a considerable degree of band dispersion is observed in both the CB and VB. The CBM of the cubic phase is more parabolic, *i.e.*, significantly dispersive, than the VBM. Therefore, for both cases of $CsCdBr_3$, the electron effective mass $\left(m_e^*\right)$ should be lower than the hole effective mass $\left(m_h^*\right)$. It results in higher electrical conductivities, which is itself a result of higher electron mobilities. In contrast, the flat band of the VBM indicates a higher hole effective mass. Hence, it is expected that the ratio of hole and electron effective mass will be higher; therefore, the electron–hole recombination rate will be lower, which is one of the key factors for photocatalytic activity. The effective mass is lower and mobility is greater for the cubic phase because the band dispersion is larger than for the hexagonal phase. The heavy hole (HH), light hole (LH), and split-off band are clearly distinguished in the hexagonal band structure, hence intra-band transition may occur and strongly contribute to the thermoelectric performance of this phase. We also calculate the effective masses of electrons and holes to support the above explanation by the parabolic band approximation method, which is discussed elsewhere.[13] The calculated value of the

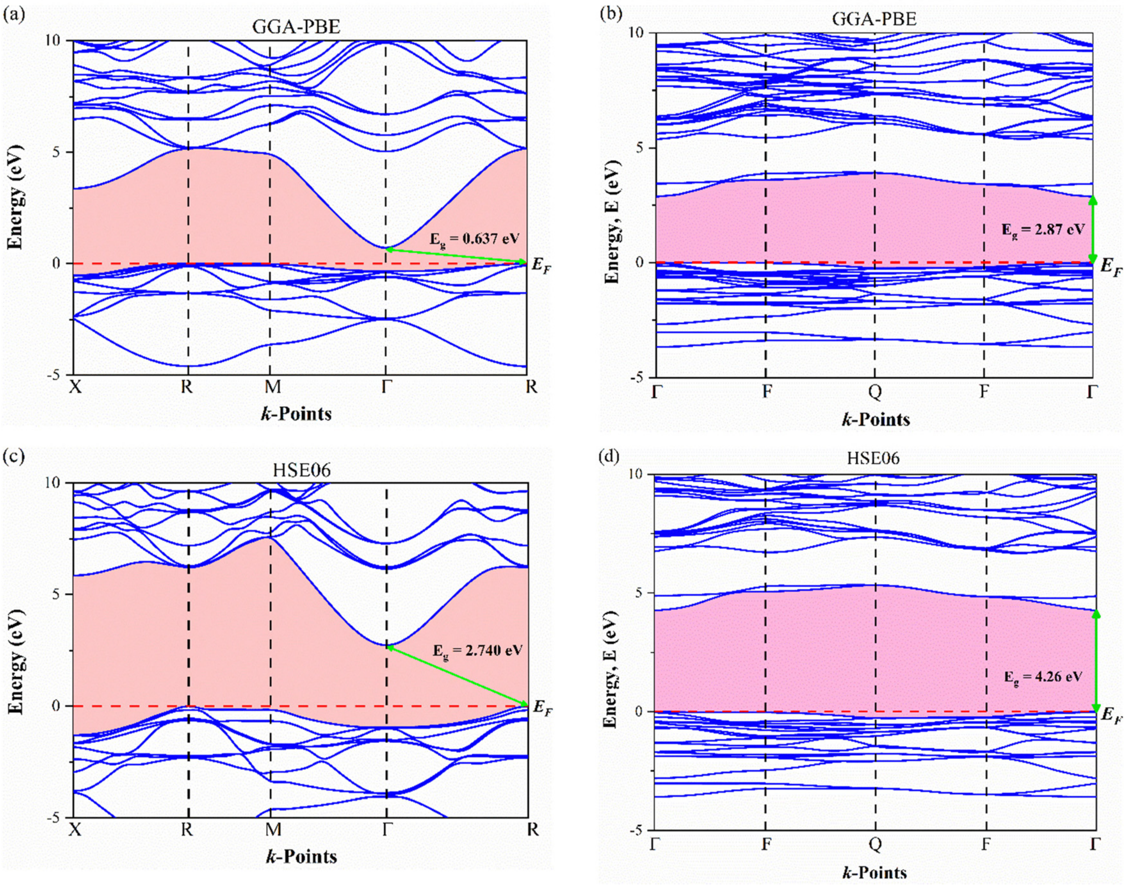

Fig. 3 Electronic band structure of the (a) and (c) cubic and (b) and (d) hexagonal phases of $CsCdBr_3$ along the high symmetry directions using GGA and HSE06 functionals.

Table 2 The calculated bandgap values E_g (eV) of the $CsCdBr_3$ polymorphs found in this study compared with the other available values

Compound	Phase	GGA-PBE	HSE06	Ref.
$CsCdBr_3$	Cubic	0.637	2.740	This work
		0.656	—	68
	Hexagonal	2.87	4.26	This work
		$4.1^{\text{expt.}}$		62
$CsPbI_3$	Cubic	1.88	—	67
	Cubic	1.19	—	28
$CsPbBr_3$	Cubic	—	2.42	69
$BaTiO_3$	Cubic	1.746	3.254	11
	Hexagonal	1.787	3.388	

electron effective mass (m_e^*) for the cubic structure at the Γ-symmetry point is $0.274m_0$ and the hole effective mass (m_h^*) at the *R*-symmetry point is $-0.603m_0$. For the hexagonal structure, the values of m_e^* and m_h^* are found to be $1.603m_0$ and $-3.541m_0$, respectively. The lower electron effective mass in the cubic phase is related to higher electron mobility and, consequently, higher electrical conductivity, if scattering rates are comparable. However, the actual mobility will depend on temperature-dependent scattering processes specific to each phase.

The computed total and partial density of states (TDOS and PDOS, respectively) of the cubic and hexagonal phases of $CsCdBr_3$ are depicted in Fig. 4(a) and (b), as a function of energy. The Fermi level, E_F, is indicated by the vertical dashed line. Several optoelectronic properties of crystals are tied to the features of the density of states (DOS), including conductivity, magnetic order, and atomic contribution to the bonding and anti-bonding states. Hybridization among different states can also be described by PDOS. For both cubic and hexagonal phases, the valence band near E_F (~ -5 to 0 eV) is mainly dominated by the presence of the Br-4p state ($\sim$11.2 electrons per eV for cubic and $\sim$22.7 electrons per eV for hexagonal) with minor antibonding contributions from Cd-4p/4d, while the conduction band is dominated by Cd-5s ($\sim$0.29–0.70 electrons per eV for cubic and $\sim$2.68 electrons per eV for hexagonal), with negligible Cs contributions ($<$0.2 electrons per eV for cubic and $<$0.6 electrons per eV for the hexagonal phase), as depicted in Fig. 4(a) and (b). Therefore, electron transitions are chiefly controlled by the transition from the Br-4p state to the Cd-5s and Cd-4p states.

While the peak positions in TDOS are similar, the hexagonal phase shows higher DOS intensity due to a greater number of atoms in the hexagonal cell arising from the existence of heavy

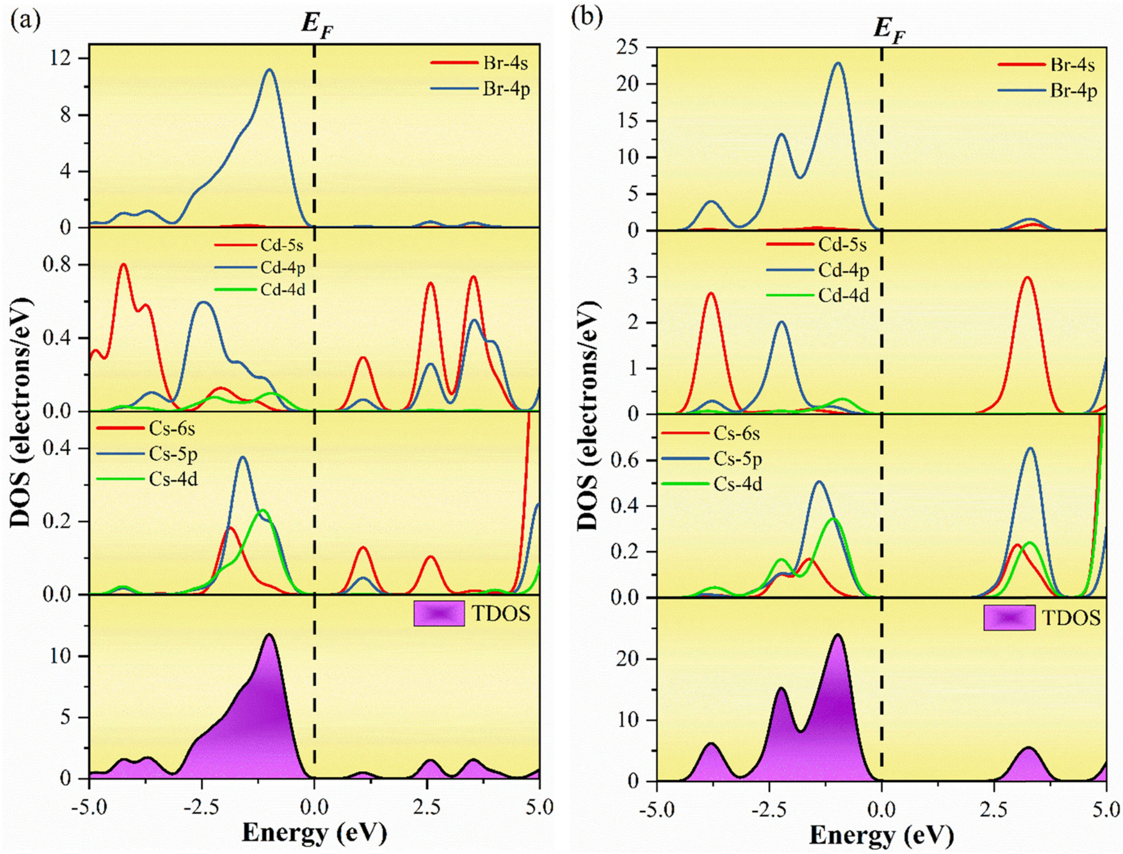

Fig. 4 Total and partial DOS of the (a) cubic and (b) hexagonal phases of $CsCdBr_3$.

hole (HH), light hole (LH), and the split-off band. The density of states varies based on dimensionality and crystallographic orientation, impacting the electronic properties of different compounds. The higher magnitude of the DOS in the hexagonal phase primarily originates from its larger unit cell (more atoms) and the presence of flatter bands, indicating a higher effective mass for carriers.

3.3 Redox potentials

In photocatalytic water splitting applications, accurate band edge location is crucial. The CBM must be above the hydrogen evolution reaction (HER) potential, and the VBM must be below the oxygen evolution reaction (OER) potential. This proper alignment means that the photocatalyst can efficiently drive both redox reactions required for water splitting. The theoretical VBM and CBM locations are calculated using the following formulae:[75]

$$E_{CB} = X - E_e - \frac{1}{2}E_g$$

$$E_{VB} = E_{CB} + E_g$$

where E_{CB} and E_{VB} indicate the corresponding CBM and VBM potential, X is the absolute electronegativity, E_g is the bandgap value, and E_e is the energy of free electrons, which is 4.5 eV on the hydrogen scale. The value of X can be calculated taking the geometric mean of the elements' mean electron affinity and electronegativity using the following formula:[11,76]

$$X = \sqrt[n]{X_1 \times X_2 \times \ldots \times X_n}$$

where X_1, X_2, *etc.* are the average of the electron affinity and electronegativity of an element.

The calculated absolute electronegativity, X, of $CsCdBr_3$ is 5.33 eV. The band edge potentials of the VB and CB of the cubic and hexagonal phases of $CsCdBr_3$ are shown in Fig. 5. Here, the CBM values are −0.54 eV and −1.30 eV for the cubic and the hexagonal phases, respectively. So, H^+ to H_2 reduction is possible since both phases have negative values of the CBM potentials. On the other hand, the VBM values are 2.20 eV and 2.96 eV for the respective phases. They are higher than 1.23 eV of O_2/H_2O, which is required for the development of O_2 from the water. These polymorphs have greater VBM potential than regularly used semiconductors such as GaAs, $BaTiO_3$, ZnSe, CdSe, Cu_2O, Ta_3N_5, *etc.*[11,77] Thus, these two $CsCdBr_3$ polymorphs are possible candidates for photocatalysts that can be used for the degradation of several carbon-based biological contaminants into biodegradable compounds and for splitting H_2O into H_2 and O_2, utilizing photogenerated electron–hole pairs under the solar radiation than similar perovskites like $CsPbI_3$.[28] From Fig. 5, it is apparent that the cubic phase possesses the highest photocatalytic performance than that of the hexagonal phase. Although the band structure reveals that

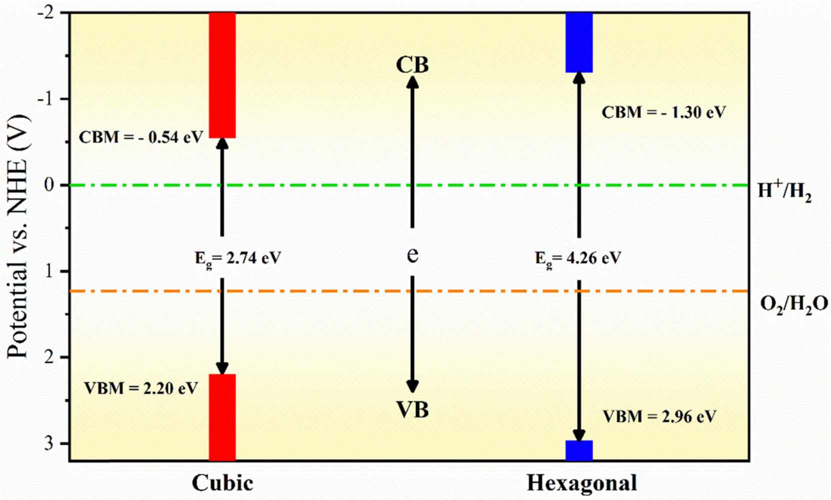

Fig. 5 Calculated band edge (CBM and VBM) potentials of the cubic and hexagonal phases of $CsCdBr_3$.

Table 3 Charge spilling parameter (%), orbital charges (electron), atomic Mulliken charges (electron), effective valence (electron), and Hirshfeld charge (electron)

$CsCdBr_3$ polymorph	Charge spilling	Species	Mulliken atomic populations s	p	d	Total	Mulliken charge	Formal ionic charge	Effective valence	Hirshfeld charge	Effective valence
Cubic	0.09	Cs	2.16	6.28	0.29	8.73	0.27	+1	0.73	0.17	0.83
		Cd	0.87	1.04	9.99	11.90	0.10	+2	1.90	0.42	1.58
		Br	1.68	5.44	—	7.12	−0.12	−1	—	−0.20	—
Hexagonal	0.09	Cs	2.07	6.12	0.24	8.43	0.57	+1	0.43	0.21	0.79
		Cd	0.95	1.00	10.00	11.94	0.06	+2	1.94	0.35	1.65
		Br	1.79	5.42	—	7.21	−0.21	−1	—	−0.19	—

the hexagonal phase has a direct bandgap, the bandgap value in the UV region restricts its uses. Doping is a common strategy to enhance photocatalytic performance by modifying band edges or reducing recombination rates, as demonstrated in similar compounds.[75]

3.4 Bond population analysis and electronic charge density

The Mulliken population analysis (MPA),[78] one of the most commonly used techniques, was used to evaluate the bonding characteristics of the two $CsCdBr_3$ polymorphs. The charge spilling parameter of the cubic and hexagonal structures is found to be 0.09 (Table 3), which implies excellent electronic bonds. The Cd atom has a greater charge than that of the Cs and Br atoms because of the main contribution from the 4d state. The deviation from formal ionic charges (Cs: +1, Cd: +2, and Br: −1) indicates a mixed ionic–covalent bonding character. This is a hallmark of most halide perovskites. The charge transfer from Cs/Cd to Br is not complete, which means the bonds have a significant degree of electron sharing (covalency). Pitriana *et al.*[79] found the existence of partial ionic and covalent bonding character in the $CsPbBr_3$ system. Table 3 also demonstrates that the effective valences of Cs and Cd atoms in $CsCdBr_3$ are non-zero, which is an indication of the presence of both ionic and covalent bonds. It can be included that the degree of covalency is higher in both polymorphs. We also employed the Hirshfeld population analysis (HPA)[80] technique to refine our calculation of bonding characteristics. Hirshfeld charge analysis suggests that electrons are transported from Cs and Cd to Br atoms. Both methods indicate that bonds are predominantly covalent with moderate ionic character, which is consistent with halide perovskites.

Table 4 shows both positive and negative values of population in both polymorphs. So, both bonding and anti-bonding type interactions are present.[81] Cs–Br shows anti-bonding type and Cd–Br shows bonding type interactions in both polymorphs. The Cd–Br bond length in the hexagonal structure is longer compared to the cubic structure. The number of bonds is also more for the hexagonal structure. These results revealed that covalent bonds mainly contribute to the formation of the crystal structures of the polymorphs, with a small amount of ionic bonds also present in both structures.

The charge density and its distribution plot offer valuable insights into the bonding characteristics of a compound. This

Table 4 Calculated total number of bonds n^{μ}, Mulliken overlap population P^{μ}, and bond length d^{μ} (Å) of the $CsCdBr_3$ polymorphs

$CsCdBr_3$ polymorphs	Bond	n^{μ}	P^{μ}	d^{μ}
Cubic	Cs–Br	3	−0.10	3.978
	Cd–Br	3	0.32	2.813
Hexagonal	Cs–Br	6, 6	−0.19, −0.07	4.170, 3.949
	Cd–Br	12	0.10	2.825

plot provides a visual representation of the spatial distribution of electrons within the compound, which is directly related to the nature and strength of the chemical bonds. Fig. 6 depicts the charge density distribution (in e Å^{-3}) for the cubic and hexagonal phases of $CsCdBr_3$ in the (110) crystallographic plane. The scale bar for the charge density ranges from 0.0 to 4.0 e Å^{-3}. In the charge density distribution mapping, the color scheme used provides a visual representation of the charge accumulation and depletion within the $CsCdBr_3$ polymorphs. Both under-investigation polymorphs have shown an asymmetric charge distribution for different atomic species.

For the cubic phase, the electronic charge around the Cd atom is very high in the (110) plane, whereas a moderate amount of charge is present at the corners around Cs atoms. The degree of charge of the Br atoms is identical to that of the Cs atoms. There is a share of charge between the Cd and Br atoms, which indicates the covalent bonding nature. For the hexagonal phase, the degree of charge of the atom species is identical to that of the cubic phase. The Cd atoms have the highest charge density, while the Cs and Br atoms have moderate charge densities. Charge density around the Cd atoms is slightly distorted in this structure. There is also charge sharing between the Cd and Br atoms. So, the bonding in $CsCdBr_3$ should be mainly covalent, with a slight ionic bonding present.

3.5 Optical properties

Knowing the optical properties of a material helps us to determine whether it can be used for the synthesis of optoelectronic and photovoltaic devices. Several optical properties, such as dielectric function, absorption coefficient, reflectivity, refractive index, optical conductivity, and electron energy loss function, of the cubic and hexagonal phases of $CsCdBr_3$ have been evaluated for photon energies of up to 30 eV using the independent particle approximation. The cubic phase is found to be optically isotropic in nature, whereas the hexagonal phase shows anisotropy. For the hexagonal phase, all calculations are performed for two polarization directions, ⟨100⟩ and ⟨001⟩ of the electric field vector.

The complex dielectric function $\varepsilon(\omega) = \varepsilon_1(\omega) + i\varepsilon_2(\omega)$ is a response function that describes how a material could respond to EM radiation in the infrared (IR), visible, and ultraviolet (UV) regions.[82] Fig. 7(a) and (b) represent the real (ε_1) and the imaginary part of the dielectric functions (ε_2) for the cubic and hexagonal structures of $CsCdBr_3$, respectively.

The static dielectric constants, also known as zero-frequency dielectric constants, can be found in Fig. 7(a). As can be seen from the figure, the cubic structure has a higher static dielectric constant (∼4.4) as compared to the hexagonal structure (∼3.5), which shows very little anisotropy. From Fig. 7(a), it can also be seen that the cubic phase has two highly intense peaks at 1.30 and 3.39 eV, respectively. In the case of the hexagonal phase, it has two intense peaks of similar intensity for the ⟨100⟩ direction at 3.52 and 5.07 eV, whereas for the ⟨001⟩ direction, the most intense peak is found at 3.90 eV. This confirms that the hexagonal structure indeed possesses strong optical anisotropy. The peaks are caused by the inter-band transition of electrons mainly from the Br-4p states of the VB to the Cd-5s states of the CB. The next peaks are due to the electronic states of Cs atoms. $\varepsilon_1(\omega)$ becomes negative two times for the cubic phase and hexagonal phase's ⟨100⟩ direction, whereas it goes negative

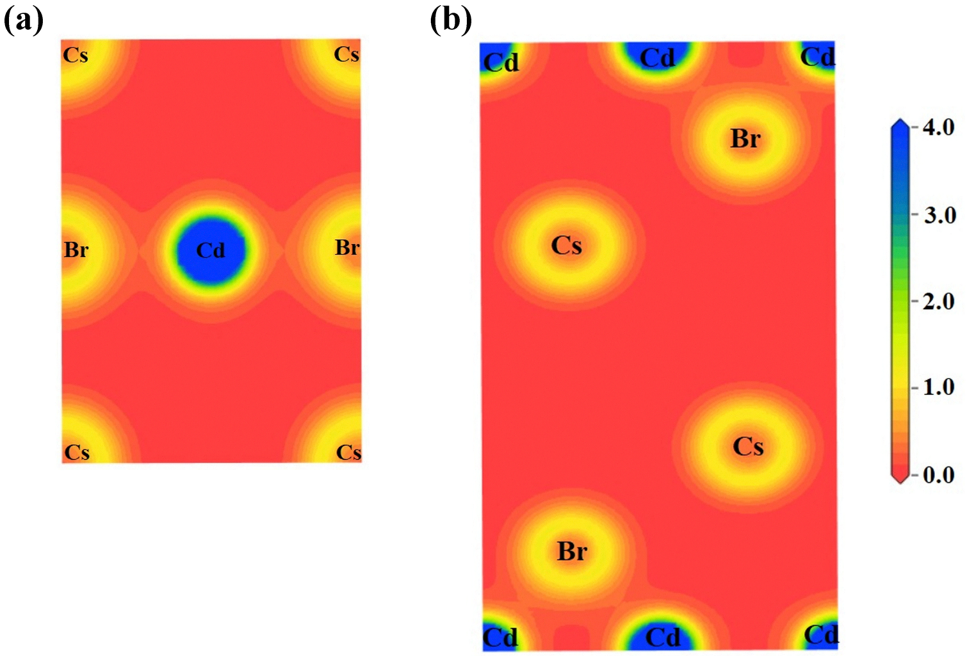

Fig. 6 Charge density distribution in the (110) plane for the (a) cubic and (b) hexagonal phases of $CsCdBr_3$. The charge density scale is shown on the upper-right.

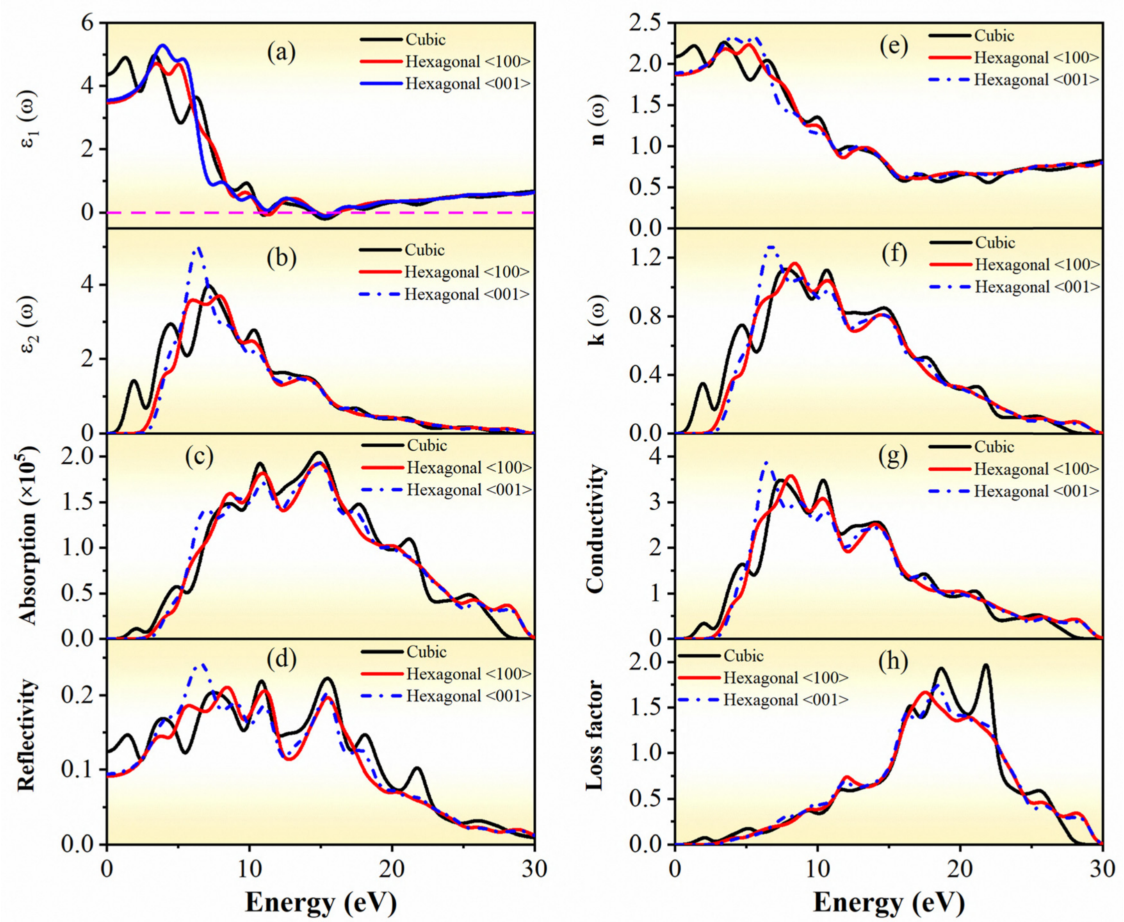

Fig. 7 (a) $\varepsilon_1(\omega)$, (b) $\varepsilon_2(\omega)$, (c) absorption coefficient, (d) reflectivity, (e) $n(\omega)$, (f) $k(\omega)$, (g) optical conductivity, and (h) energy loss function of the cubic and hexagonal phases of $CsCdBr_3$ as a function of photon energy.

only one time for the ⟨001⟩ direction of the hexagonal phase. For the cubic phase, there are several $\varepsilon_2(\omega)$ peaks found, and the most prominent peak is found at 7.15 eV. The hexagonal phase for the ⟨100⟩ direction shows two intense peaks at 6.10 and 7.97 eV. The hexagonal phase for the ⟨001⟩ direction shows only one intense peak at 6.30 eV, and this peak is the highest between the two phases. After the peaks, the value of $\varepsilon_2(\omega)$ decreases gradually.

Energy dependent absorption coefficient $\alpha(\omega)$ for the cubic and hexagonal phases of $CsCdBr_3$ is depicted in Fig. 7(c). It quantifies how much light at a specific wavelength can be absorbed by the compound. As seen, the absorption spectra do not begin at zero photon energy, which is an indicator of semiconducting compounds.[11] The value of the absorption coefficient is high ($\sim 10^5$ cm^{-1}) in the UV region, and it stays high (60% of the peak) between ~7.05 eV and ~18.18 eV. This is comparable with the likes of $CsPbI_3$ and $BaTiO_3$ (10^4–10^5 cm^{-1}),[11,67] which are also candidates for solar cell applications. The higher value of absorbance also suggests good solar energy conversion ability. So, this compound can be a good solar energy absorber in the mid-UV region. Moreover, optical anisotropy is less for this property.

Reflectivity, $R(\omega)$, of any material represents the fraction of incident light energy that is reflected back. Energy-dependent reflectivity, $R(\omega)$, for the two phases of $CsCdBr_3$ is depicted in Fig. 7(d). It is seen that there is moderate anisotropy present. For the cubic phase, reflectivity at 0 eV energy is ~60% of the peak. In the visible range, it starts decreasing at first and then increases to 68%. It follows some peaks in the UV region, and the peak value is found at ~15.45 eV. The hexagonal phase in the ⟨100⟩ direction has a more or less similar pattern compared with the cubic phase. For the ⟨001⟩ direction, the peak value is found at ~6.47 eV. As a whole, the reflectivity spectra suggest that both phases of this compound have the potential to be used as a reflector material in the visible and near-IR to mid-UV region. The value of R is very low (~20%) in the whole spectral range, hence both phases can be a good candidate for anti-reflection coating material. Since the absorbance and reflectance are lower in the IR-visible region, both phases should have higher transmittance, which is very common for wide bandgap semiconductors.[12,83,84]

The refractive index, $N(\omega)$, is a complex quantity and it comprises two parts. The real part of the refractive index, $n(\omega)$, governs the group velocity of light waves within a material. On the other hand, the imaginary part, $k(\omega)$, also known as the extinction coefficient, determines the attenuation of light waves when passing through a material. $k(\omega)$ is also correlated to the dielectric function and absorption coefficient.[85] The calculated values of the real and imaginary parts of the refractive index are shown in Fig. 7(e) and (f), respectively. $n(\omega)$ actually has an inverse relation with the electronic bandgap, and that is confirmed by the $n(0)$ values. $n(0)$ is found to be 2.67 for the cubic phase, whereas it is found to be 1.87 and 1.89 for the $\langle 100\rangle$ and $\langle 001\rangle$ directions of the hexagonal phase, respectively. The refractive index of the cubic phase exhibits the prime peaks in both the IR and visible regions, which gradually diminish in the UV region, as seen in Fig. 7(e). For the hexagonal phase, the prime peaks are found near the UV region. At higher energies ($>\sim$14 eV), anisotropy vanishes because the effect of polarizabilities diminishes with higher frequency. A moderate value of $n(\omega)$ indicates that it could be used to build light emitting devices. The peak values of $k(\omega)$ are found in the UV region for both polymorphs, which again suggests they could be good UV absorbers. The strong optical anisotropy in the hexagonal phase is highlighted as a unique feature for designing polarization-sensitive optoelectronic devices.

Optical conductivity, plotted in Fig. 7(g), does not start at zero energy as expected since both polymorphs are semiconductors. The cubic phase exhibits two comparable high peaks at $\sim$7.43 and $\sim$10.35 eV. In the case of the hexagonal phase, conductivity is higher for the $\langle 001\rangle$ direction, and the highest peaks are found at $\sim$6.45 and $\sim$8.10 eV for the $\langle 001\rangle$ and $\langle 100\rangle$ directions, respectively. After that, a dip in conductivity is observed. The anisotropy found in the hexagonal phase disappears after $\sim$18.40 eV.

The calculated loss function for the two phases of $CsCdBr_3$ is shown in Fig. 7(h). We see that the peaks of $L(\omega)$ occur at 21.81 eV, 17.55 eV, and 18.42 eV, respectively, for the cubic, hexagonal $\langle 100\rangle$, and hexagonal $\langle 001\rangle$ phase. The peaks of $L(\omega)$ are found at the trailing edge of the reflectivity spectra. Both phases have similar patterns for the loss function, though they have anomalies in the region of peaks. For the hexagonal phase, anisotropy vanishes after the peak is reached. In summary, the high absorption coefficients ($>10^5$ cm^{-1}) in the UV region with a combination of low reflectivity ($<$20%) make the polymorphs, particularly the anisotropic hexagonal phase, excellent candidates for UV-selective photodetectors and antireflection coatings.

3.6 Elastic properties

Table 5 presents the elastic properties of the cubic and hexagonal structures of $CsCdBr_3$. From the calculated elastic stiffness constants C_{ij}, the mechanical stability of the materials under study can be estimated using the stability requirements of the Born–Huang criteria,[86] which are given below:

For a cubic system,

$$C_{11} > 0,\quad C_{44} > 0;\quad C_{11} > B > C_{12};\quad (C_{11} - C_{12}) > 0;\quad (C_{11} + 2C_{12}) > 0;$$

and for a hexagonal system,

$$C_{11} > |C_{12}|;\quad 2{C_{13}}^2 < C_{33}(C_{11} + C_{12});\quad C_{44} > 0;\quad C_{66} > 0.$$

Table 5 The calculated stiffness constants C_{ij} (GPa) and Cauchy pressure C_P (GPa) of the cubic and hexagonal phases of $CsCdBr_3$, respectively

$CsCdBr_3$ polymorph	C_{11}	C_{12}	C_{13}	C_{33}	C_{44}	C_P
Cubic	42.81	14.53	14.53	42.81	9.82	4.71
Hexagonal	17.45	7.23	5.10	29.14	2.11	5.12, 2.99

The mechanical stability of polymorphs shows how they withstand diverse mechanical changes. Along with the chemical stability criterion, Table 5 demonstrates that these conditions are met, and so all polymorphs are mechanically stable.

The estimated values of Cauchy pressure, C_P, for the cubic and hexagonal phases using their corresponding equation[87] are presented in Table 5. It is a stress property of materials that quantifies the ductility or brittleness of a material. The ductility and presence of an ionic bond in a compound are probable when the Cauchy pressure is positive, and *vice versa*. The positive nature of C_P results in the ductility and predominance of ionic bonding in both cubic and hexagonal phases of $CsCdBr_3$. The ductile behavior of the investigated polymorphs is practically important since it can be exploited to produce high-quality thin films.[88]

The bulk modulus (B) reflects a material's resistance to pressure from the environment. From Table 6, it is seen that cubic and hexagonal structures have low values (23.96 and 10.83 GPa) of bulk modulus. So, the polymorphs are prone to volume strain. The cubic phase has a slightly higher shear modulus (11.37 GPa) than the hexagonal phase (4.22 GPa), and hence it has stronger shear resistance. Young's moduli describe the stiffness of the studied polymorphs, which is a vital elastic property. The higher the value of Young's modulus, the stiffer the material. As a result, the cubic phase is stiffer (29.45 GPa) than the hexagonal phase (11.20 GPa).

One of the key parameters of the materials that is important is their ductility or brittleness, which may be determined using their Poisson ratio (ν). If a material's Poisson ratio exceeds 0.26, it is ductile, and a value less than 0.26 indicates brittleness. Both phases of $CsCdBr_3$ had a Poisson ratio greater than 0.26, indicating that they are ductile. The assessment of Pugh's ratio (B/G)[89] confirms the ductility of the examined structures because it is more than the threshold value, 1.75. Since the value of ν is in the range 0.25–0.50, the force is central. Ductility and a dominating central force are observed in the hexagonal structure rather than the cubic structure.

Table 6 Bulk modulus B (GPa), shear modulus G (GPa), Young's modulus E (GPa), Poisson's ratio ν, and Pugh's ratio B/G of the cubic and hexagonal phases of $CsCdBr_3$, respectively, found in this study, compared with the other available values

Compound	Phase	B	G	E	ν	B/G	Ref.
$CsCdBr_3$	Cubic	23.96	11.37	29.45	0.295	2.11	This work
	Hexagonal	10.83	4.22	11.20	0.327	2.56	
$CsPbI_3$	Orthorhombic	17.852	9.218	23.593	0.279	1.936	28
	Cubic	14.80	7.06	18.26	0.294	—	67
$CsPbBr_3$	Cubic	19.43	8.31	21.69	—	2.34	69

Table 7 Density ρ (g cm^{-3}), machinability index μ_M, Debye temperature θ_D (K), melting temperature T_m (K), minimum thermal conductivity k_{min} (W m^{-1} K^{-1}), the Grüneisen parameter γ, hardness values H_{macro} and H_{micro} (GPa), and fracture toughness K_{IC} (MPa m$^{0.5}$) of the cubic and hexagonal phases of CsCdBr$_3$, respectively

Phase	ρ	μ_M	θ_D	T_m	k_{min}	γ	H_{macro}	H_{micro}	K_{IC}
Cubic	4.52	2.440	210.89	546.66	0.226	1.743	0.466	1.552	0.261
Hexagonal	4.30	5.138	98.86	450.05	0.218	1.956	−1.456	0.486	0.124

Between the two phases, the cubic phase is denser with a density of 4.52 g cm^{-3}. It is also confirmed by the average acoustic velocity, which is also higher in the cubic structure, and acoustic velocity is directly proportional to the density of a compound. The machinability index, μ_M, of a material is a dependable measure of its competence. Moreover, it is beneficial for measuring the plasticity[90] and lubricating characteristics of a substance. The calculation of μ_M is conducted using the following equation: $\mu_M = B/C_{44}$, where B is the bulk modulus. Table 7 reports the μ_M of the cubic and hexagonal phases of CsCdBr$_3$, and based on our findings, the hexagonal phase is two times more appropriate for use in manufactured machines.

Table 7 illustrates that the calculated Debye temperature, θ_D, of the cubic phase is 210.89 K, which is two times higher than that of the hexagonal phase (98.86 K). The Debye temperature can also be used to determine the rigidity of covalent bonds throughout materials.[91] Therefore, it is reasonable to expect that the cubic phase has stronger covalent bonds than the hexagonal phase. The Debye temperature is directly interrelated to the melting temperature (Table 7), which is usually the case for these polymorphs too.[92] The melting temperature T_m of solids can be determined with the help of the following equation:[93]

$$T_m = 354\ \text{K} + \left(4.5\ \text{K GPa}^{-1}\right)\left(\frac{2C_{11} + C_{33}}{3}\right) \pm 300\ \text{K}$$

The melting temperature of the cubic phase is higher than that of the hexagonal phase. The Debye temperature is related to the lattice thermal conductivity. Since the value of θ_D is low for both compounds, they should exhibit low thermal conductivity.

The minimum thermal conductivity k_{min} of the cubic and hexagonal phases of CsCdBr$_3$ can be determined using Clarke's formula.[94] It is important to remember that not all materials need to have a high value of thermal conductivity, as they can be used in thermoelectric devices or insulation. Both CsCdBr$_3$ polymorphs can be utilized as thermal barrier coating materials (TBC), as the k_{min} of these polymorphs is much less than the limitation value of 1.25 W m^{-1} K^{-1}.[95]

The Grüneisen parameter (γ) is a function of both volume and temperature and is directly associated with the strength of phonon–phonon interaction. This parameter displays several key characteristics of a material, such as thermal conductivity and expansion due to thermal energy, the temperature dependence of elastic properties, attenuation of acoustic waves, and the measurement of the anharmonicity of the bonds in a crystal. The calculated values of γ for the cubic and hexagonal forms of CsCdBr$_3$ are 1.74 and 1.95, respectively. The presence of strong anharmonicity in the lattice vibration was indicated by the predicted high values of γ (Table 7), which suggests that both compounds will have low thermal conductivity. Furthermore, high values of γ show that the compound's thermal properties, such as thermal conductivity, specific heat, and thermal expansion, are highly sensitive to changes in pressure and temperature.

The hardness of CsCdBr$_3$ polymorphs was determined by the application of the presented formulae:

$$H_{macro} = 2\left[\left(\frac{G}{B}\right)^2 G\right]^{0.585} - 3$$

$$H_{micro} = \frac{(1-2\upsilon)E}{6(1+\upsilon)}$$

Their resistance to notching pressures is directly impacted by the highly interdependent connection between hardness and crystalline elastic modulus. From Table 7, it is anticipated that both polymorphs are soft materials as seen by their respective hardness values. Between the two polymorphs, the cubic phase is slightly harder, considering the stated value (H_{micro} = 1.55 GPa), whereas the hexagonal phase has a low hardness value (H_{micro} = 0.49 GPa). So, the polymorphs show a soft nature, and the hexagonal phase possesses extreme softness.[96]

Fracture toughness, K_{IC}, which measures a material's ability to resist an external force causing cracks and fractures to spread, can be calculated using the formula published by Niu *et al.*:[97]

$$K_{IC} = V_0^{\frac{1}{6}} G \left(\frac{B}{G}\right)^{0.5}$$

The constant V_0 is the final volume per atom of the optimized unit cell, and the estimated value of K_{IC} of CsCdBr$_3$ polymorphs is shown in Table 7. Although the fracture toughness value is low for both polymorphs, the superior fracture toughness of the cubic phase compared to the hexagonal phase allows it to tolerate greater pressures without undergoing crack propagation.

As a whole, the low values of the bulk and shear moduli, high Pugh's ratio (>1.75), and high Poisson's ratio (>0.26) give clear indications that both polymorphs are soft and ductile. This mechanical profile is highly advantageous for processing and fabricating flexible thin-film devices, as it reduces the risk of cracking under stress.

3.7 Thermoelectric properties

The physical phenomena that occur within a thermoelectric device contribute to the thermoelectric influence. It can produce an electric voltage from the temperature gradient. The thermoelectric influence is a generic operation based on three well-known principles: the Seebeck, Peltier, and Thomson effects. The Seebeck coefficient, electrical conductivity, and thermal conductivity of a thermoelectric material are the main parameters controlling its performance in thermoelectric (TE) devices. We used the Boltzmann semiclassical transport theory, implemented in the BoltzTrap2 scheme, to calculate the thermoelectric properties of $CsCdBr_3$ polymorphs with a constant relaxation time approximation. Fig. 8 illustrates how the thermoelectric characteristics of the cubic and hexagonal polymorphs of $CsCdBr_3$ vary with chemical potential (μ) at different temperatures.

Fig. 8(a) and (b) illustrate the Seebeck coefficient (S) as a function of chemical potential (μ) ranging from −1.45 to 1.45 eV for the cubic phase, and −2.15 to 2.15 eV for the hexagonal polymorph of $CsCdBr_3$, respectively, at temperatures of 300, 450, 600, 750, and 900 K. In the cubic phase, S peaks are concentrated near ∼0 eV, while the hexagonal phase exhibits five distinct peaks within the −0.95 to 1.05 eV region. At 300 K, the cubic phase demonstrates maximum S values of 1330 $\mu V\ K^{-1}$ for p-type and −1140 $\mu V\ K^{-1}$ for n-type behavior. There is a notable asymmetry and offset between the positive and negative peaks, suggesting anisotropic transport properties characteristic of hexagonal structures. The hexagonal phase displays peaks at different energy levels for p-type and n-type behaviors, with maximum S values reaching 1575 $\mu V\ K^{-1}$ and −1575 $\mu V\ K^{-1}$, respectively. The wider separation between positive and negative peaks indicates a larger bandgap compared to the cubic structure. At higher temperatures, the peak value of S decreases with increasing temperature for the cubic phase. The values of S (Fig. 8a) at 450, 600, 750, and 900 K are 950 $\mu V\ K^{-1}$ (−650 $\mu V\ K^{-1}$), 760 $\mu V\ K^{-1}$ (−670 $\mu V\ K^{-1}$), 630 $\mu V\ K^{-1}$ (−360 $\mu V\ K^{-1}$), and 550 $\mu V\ K^{-1}$ (−290 $\mu V\ K^{-1}$) in the p- (n-)region, respectively. On the other hand, for the hexagonal structure, the value of S shifted its maximum position equally toward the Fermi level with increasing temperature. The above results concluded that both p-type and n-type doping can be effective, and the optimal doping type depends on the temperature and the specific phase. Besides, the preferred type of doping also depends on the electrical and thermal

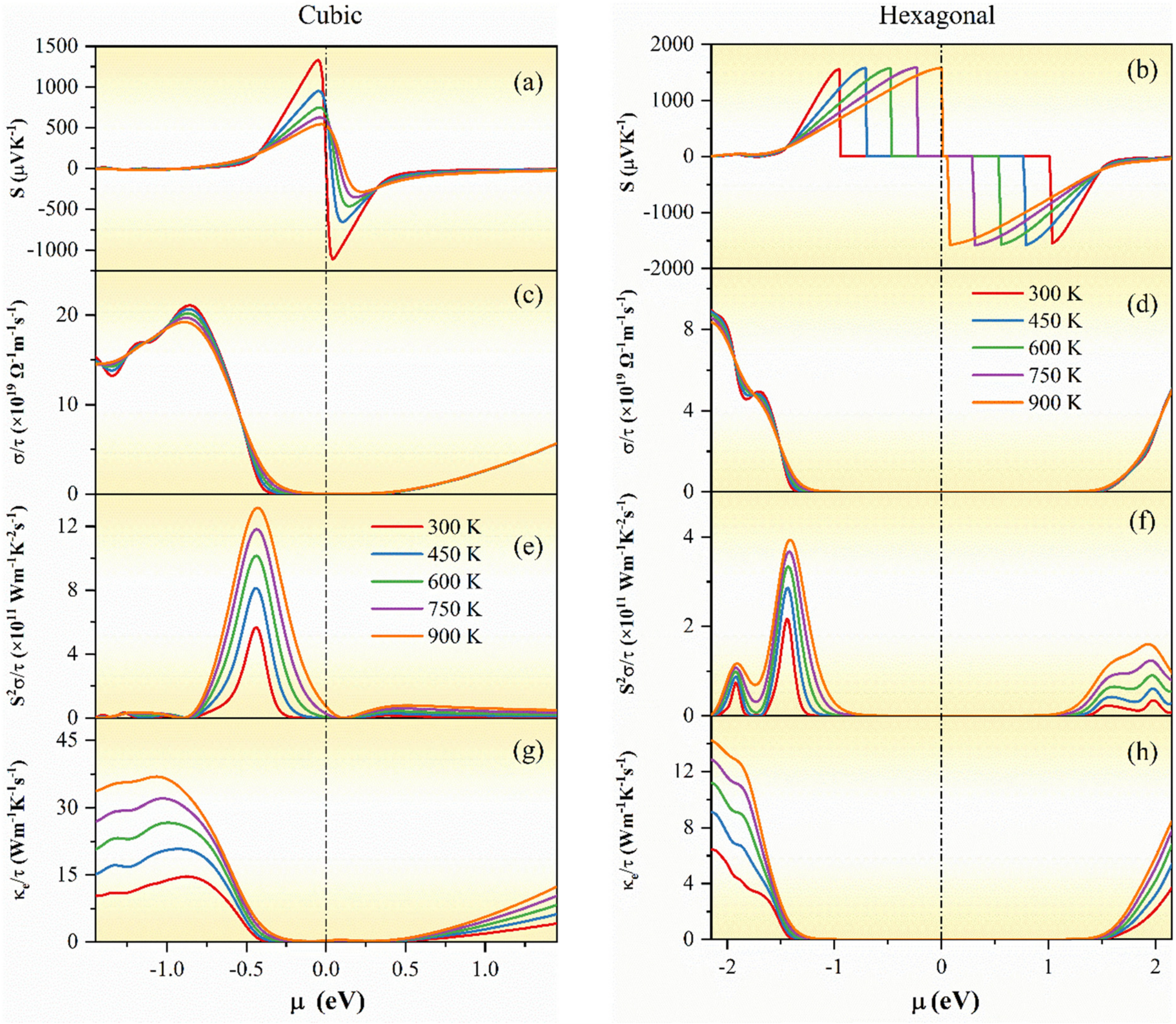

Fig. 8 Variation of the (a) and (b) Seebeck coefficient, S, (c) and (d) electrical conductivity, σ/τ, (e) and (f) power factor, $S^2\sigma/\tau$, and (g) and (h) electronic thermal conductivity, κ_e/τ, of the cubic and hexagonal phases of $CsCdBr_3$ respectively, as a function of chemical potential, μ.

conductivity. Aliovalent doping (*e.g.*, partial substitution of Cd^{2+} with In^{3+} or Na^{+} for n-type or p-type conduction, respectively) could be employed to tune the carrier concentration without drastically altering the band edges. This is crucial for optimizing the thermoelectric performance beyond intrinsic thermal excitation.

The analysis of electrical conductivity (σ/τ) across different temperature ranges provides insights into the thermoelectric performance of $CsCdBr_3$. Fig. 8(c) and (d) illustrate how electrical conductivity varies with chemical potential at multiple temperatures. Electrical conductivity shows temperature dependence at the studied temperatures (300, 450, 600, 750, and 900 K). Chemical potential variations primarily shape the conductivity profile, but temperature also significantly influences its magnitude, due to increased carrier excitation. Since the electrical conductivity is linearly related to the carrier concentrations and carrier concentrations are exponentially related to temperature, a significant change in temperature causes a considerable change in electrical conductivity. The electrical conductivity profiles of the $CsCdBr_3$ polymorphs differ, showing minimal conductivity in the bandgap region. In an intrinsic semiconductor, electrical conductivity is very low within the bandgap because the density of states is minimal. It results in a few thermally excited electron–hole pairs as carriers. However, conductivity increases with increasing chemical potential or temperature. A higher chemical potential shifts the Fermi level toward the conduction band (as in n-type doping). It increases the electron concentration and thus the number of available carriers. Similarly, higher temperatures provide greater thermal energy (k_BT), which promotes more electrons into the conduction band and thereby boosts overall conductivity. Maximum conductivity values are $21.16 \times 10^{19}\ \Omega^{-1}\ m^{-1}\ s^{-1}$ at −0.85 eV and $8.92 \times 10^{19}\ \Omega^{-1}\ m^{-1}\ s^{-1}$ at −2.15 eV for p-type cubic and hexagonal structures, respectively, which suggests the cubic phase has a potential advantage for thermoelectric applications.

The power factor (PF), defined as PF = $S^2\sigma$, represents a critical parameter for thermoelectric materials, incorporating both the Seebeck coefficient (S) and electrical conductivity (σ). Fig. 8(e) and (f) present the power factor behavior of $CsCdBr_3$ polymorphs as a function of chemical potential (μ) across various temperatures. A consistent trend emerges across both $CsCdBr_3$ polymorphs – the power factor increases with increasing temperature. The maximum values of PFs occur for 900 K, which are 13.27×10^{11} and $3.93 \times 10^{11}\ W\ m^{-1}\ K^{-2}\ s^{-1}$ at −0.42 and −1.41 eV for the cubic and hexagonal structures, respectively. Thus, in contrast to n-type zones, maximum PF is reached in p-type regions. This indicates that a higher doping density is required to obtain maximum PF for the hexagonal structure because of its wide bandgap as compared to the cubic structure.

Thermal conductivity (κ) is a measurement of the flow of carriers. There are two types of conductivity: electronic (κ_e) and phonon (κ_{ph}) thermal conductivity, which combine to form κ. TE materials are characterized by low thermal conductivity. In Fig. 8(g) and (h), the chemical potential dependent electronic thermal conductivity at various temperatures is shown. As the temperature and chemical potential increase, so does κ_e. With temperature, κ_e rises because of an increase in the energy of free electrons. As a result, vibrational energy increases too. Larger chemical potentials lead to larger electron concentrations and hence higher κ_e. The maximum values of κ_e are found to be $37.10 \times 10^{14}\ W\ m^{-1}\ K^{-1}\ s^{-1}$ at −1.05 eV and $14.27 \times 10^{14}\ W\ m^{-1}\ K^{-1}\ s^{-1}$ at −2.15 eV for the cubic and hexagonal $CsCdBr_3$ structures, respectively. The low electronic thermal conductivity is a positive indicator; however, the total thermal conductivity will be dominated by the lattice component (κ_{ph}). Generally, wide bandgap materials usually have higher lattice thermal conductivity and lower electronic contribution to total thermal conductivity.[98,99] Due to this reason, κe of the hexagonal structure is significantly lower than the cubic structure. It is also mentioned that the thermal conductivity of both polymorphs has a maximum value in the p-region.

Thermoelectric properties are also plotted as a function of temperature at the valence band maximum ($E - E_F$) and conduction band minimum ($E + E_F$), as can be seen in Fig. 9(a)–(h). At the VBM, the value of S is 80 and 224 $\mu V\ K^{-1}$ for the cubic and hexagonal polymorph of $CsCdBr_3$, respectively, whereas at the CBM, the value of S is −55 $\mu V\ K^{-1}$ and −444 $\mu V\ K^{-1}$, for the respective phases at 300 K. It is also observed that for both cases (n- and p-type), the value of S increases for cubic phases but it decreases for the hexagonal phase with increasing temperature. The value of S is comparable with the value obtained for the cubic and hexagonal phases of the $CsCdCl_3$ perovskite.[100] Our calculated value is also consistent with the value of $CsSnI_3$ structures.[101] The $CsCdCl_3$ compound also shows a similar temperature trend of Seebeck coefficient to our studied compounds.[100] The Seebeck coefficient and thermoelectric power are mostly determined by the values of ($E_{CBM} - E_F$) or ($E_F - E_{VBM}$), where E_F, E_{CBM} and E_{VBM} represent the energy of the Fermi level, conduction band minimum and valence band maximum, respectively; therefore, a larger difference yields a larger S and thermoelectric power. Due to lower crystal symmetry and greater ionic interactions, the lower temperature hexagonal phase of $CsCdBr_3$ exhibits a higher bandgap than the cubic phase. Therefore, it is expected that the hexagonal structure should have a higher value of S as compared to the cubic structure. Besides the flat valence band of the hexagonal structure which corresponds to a higher effective mass as compared to the cubic structure is another reason for its higher value of S. The hexagonal phase, with a wider effective bandgap and anisotropic bands, behaves as a non-degenerate semiconductor. As temperature increases, thermal excitation of minority carriers enhances the bipolar effect, reducing S. Besides, as the temperature rises, thermal scattering by phonons may affect the electronic transition and hence reduce the value of S. Anisotropy was observed in the hexagonal phase (Fig. S2(a)–(d)), which exhibits varying characteristics in various orientations throughout the crystal lattice. On the other hand, the cubic phase has a lower bandgap and more uniform electrical characteristics due to its greater symmetry leading to a more isotropic band structure with potentially higher carrier density and degeneracy near the Fermi level. In this regime, the

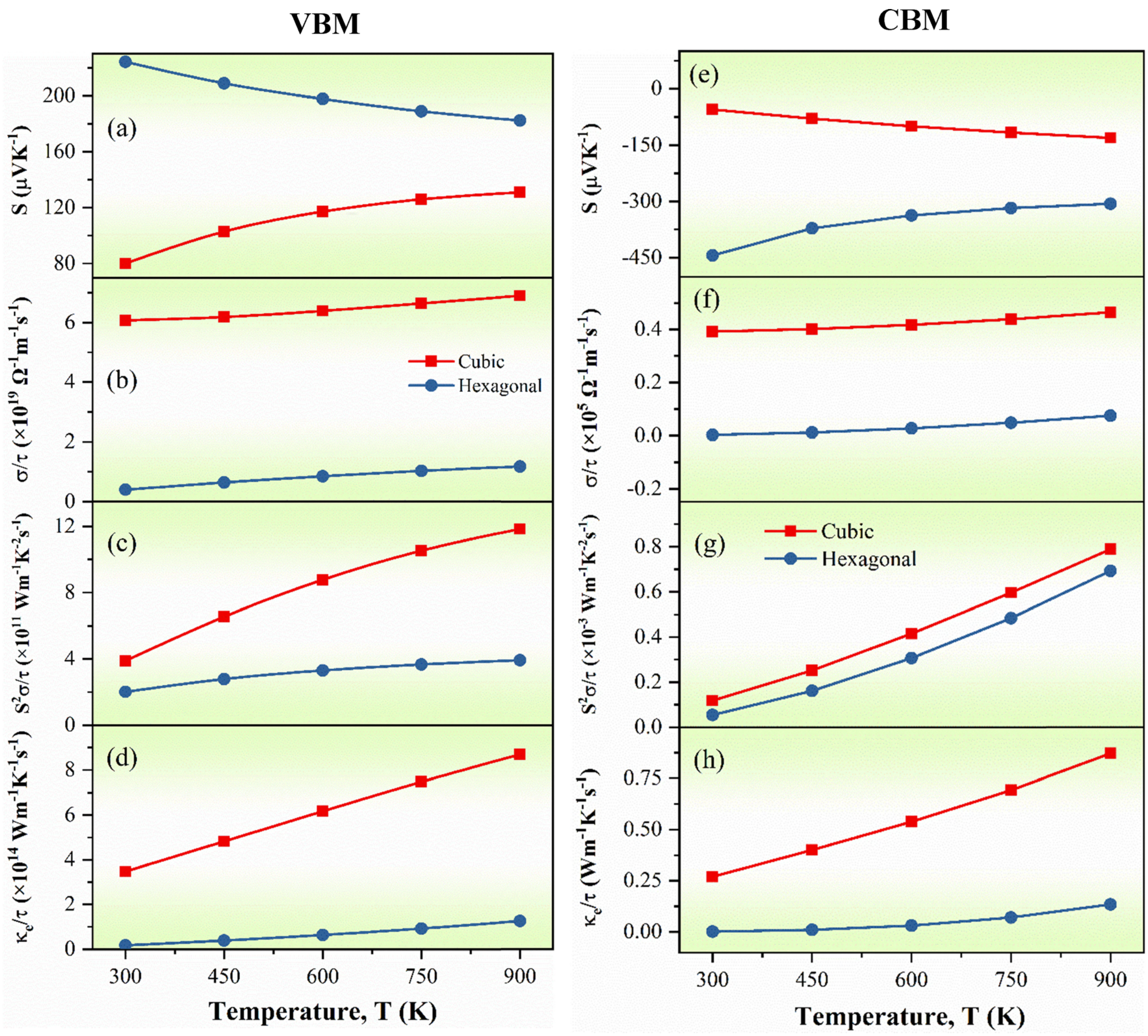

Fig. 9 Variation of the (a) and (e) Seebeck coefficient, S, (b) and (f) electrical conductivity, σ/τ, (c) and (g) power factor, $S^2\sigma/\tau$, and (d) and (h) electronic thermal conductivity, κ_e/τ, of the cubic and hexagonal phases of $CsCdBr_3$ respectively, as a function of temperature at the top of the valence band (VBM) and at the bottom of the conduction band (CBM).

material behaves closer to a degenerate semiconductor, where the Seebeck coefficient follows the Mott relation.[102] Since the carrier concentration n is weakly temperature dependent but dominated by doping or intrinsic band degeneracy rather than thermal activation, S is linearly related to T. Due to this, S increases with increasing T in the cubic structure, which is a common feature in cubic halide perovskites. In cubic $CsCdBr_3$, the high symmetry and flatter bands amplify electron–phonon coupling and increase the scattering effect, which can enhance the value of S. This contrasts with the hexagonal phase, where stronger anisotropy may lead to more localized states and reduce the value of S. However, the hexagonal structure shows a higher value of S for the whole temperature range. Electrical conductivity, σ/τ, follows the same trend for both polymorphs, and it rises slightly with temperature, which confirms the semiconducting nature. The cubic structure shows significantly higher electrical conductivity than the hexagonal structure at the VBM and CBM, respectively, and the lower thermal conductivity of the hexagonal phase is mainly responsible for the wider bandgap value compared to the cubic phase. It is also mentioned that hole-generated thermal conductivity is higher than the electron generated thermal conductivity for both phases. The power factor (PF), $S^2\sigma/\tau$, and the electronic thermal conductivity, κ_e/τ, follow the same pattern for both phases at the VBM and CBM. They increase with temperature, and the cubic phase has superior values at each temperature. The value of PF is higher for p-type character in both cases, although the value of PF is significantly higher for the cubic phase. The observed higher electronic thermal conductivity, κ_e/τ, of the cubic phase as compared to the hexagonal structure is because wide bandgap materials typically exhibit higher lattice thermal conductivity and lower electronic contribution to total thermal conductivity.[98,99] In conclusion, while the hexagonal phase has a higher S, the cubic phase is the more promising thermoelectric material due to its significantly higher electronic conductivity, σ/τ, and power factor, PF/τ, which is the key metric for performance. It is also mentioned that the p-type nature is dominating as compared to the n-type character in both phases.

4. Conclusion

The ground-state characteristics of the cubic and hexagonal polymorphs of $CsCdBr_3$ are meticulously studied in this work using DFT. In accordance with experimental findings, our structural analysis revealed that both polymorphs are stable, and the lattice constants and unit cell volumes closely mirror previously reported experimental data. Both phases have a semiconducting nature, which can be confirmed from their respective band structures, as there is a finite value of bandgap. The cubic phase has an indirect bandgap, while the hexagonal phase has a direct bandgap. The main contribution to the valence band comes from the Br-4p state, while the lower conduction band is composed of a hybridization of Cd-5s/4p and Br-4p states. The strong redox potential of $CsCdBr_3$ polymorphs makes them quite intriguing for water splitting as well as for degrading organic contaminants and color molecules. Both polymorphs show a mixed bonding nature, confirmed by their charge density distribution as well as Mulliken charge and bond analyses. The hexagonal phase is found to be optically anisotropic, whereas the cubic phase shows isotropy. Optical parameters also support the semiconducting nature of $CsCdBr_3$ polymorphs. Additionally, the optical findings indicated that the $CsCdBr_3$ polymorphs are a promising option for applications involving UV-based optical devices. Both polymorphs are found to be soft materials, and the hexagonal phase is softer. Even though both polymorphs are ductile, Poisson's and Pugh's ratios support slightly higher ductility of the hexagonal phase. Higher values of elastic moduli reveal that the cubic phase exhibits superior stiffness and resilience to the hexagonal phase. Thermoelectric properties suggest that the cubic structure is better for TE applications due to its higher PF values. Anisotropic thermoelectric properties are also found in the hexagonal phase. These findings open the door for additional experimental research and technical developments in the fields of photocatalysis, optoelectronics, and thermoelectricity by offering insightful information on the functional potential of $CsCdBr_3$ polymorphs.

Conflicts of interest

The authors declare that they have no known competing financial interests or personal relationships that could have appeared to influence the work reported in this paper.

Data availability

The data supporting this article have been included as part of the supplementary information (SI). Supplementary information: geometry optimization, elastic calculations, and population analyses are available in .txt files. Band structures, density of states (DOS), and optical properties can be found in .csv files. Thermoelectric properties are provided in .trace2 files. See DOI: https://doi.org/10.1039/d5ma00693g.

Acknowledgements

The authors acknowledge that the research grant (BSMRSTU-RC-24-031) from Gopalganj Science and Technology University, Gopalganj-8105, Bangladesh, partly supported this work.

References

1 S. Y. Chae, H. Jung, H. S. Jeon, B. K. Min, Y. J. Hwang and O.-S. Joo, Morphology control of one-dimensional heterojunctions for highly efficient photoanodes used for solar water splitting, *J. Mater. Chem. A*, 2014, **2**, 11408–11416, DOI: 10.1039/C4TA00702F.

2 I. Fujimoto, N. Wang, R. Saito, Y. Miseki, T. Gunji and K. Sayama, $WO_3/BiVO_4$ composite photoelectrode prepared by improved auto-combustion method for highly efficient water splitting, *Int. J. Hydrogen Energy*, 2014, **39**, 2454–2461, DOI: 10.1016/j.ijhydene.2013.08.114.

3 A. Kargar, Y. Jing, S. J. Kim, C. T. Riley, X. Pan and D. Wang, ZnO/CuO Heterojunction Branched Nanowires for Photoelectrochemical Hydrogen Generation, *ACS Nano*, 2013, **7**, 11112–11120, DOI: 10.1021/nn404838n.

4 M. N. H. Liton, A. Rani, M. K. R. Khan, M. S. I. Sarker, M. M. Rahman and M. Kamruzzman, Insight of the role of F-impurity on the structural, electro-optical properties of ZnO: DFT and experiment, *Mater. Sci. Semicond. Process.*, 2023, **154**, 107223, DOI: 10.1016/j.mssp.2022.107223.

5 J. Y. Kim, G. Magesh, D. H. Youn, J.-W. Jang, J. Kubota, K. Domen and J. S. Lee, Single-crystalline, wormlike hematite photoanodes for efficient solar water splitting, *Sci. Rep.*, 2013, **3**, 2681, DOI: 10.1038/srep02681.

6 R. V. Gonçalves, P. Migowski, H. Wender, D. Eberhardt, D. E. Weibel, F. C. Sonaglio, M. J. M. Zapata, J. Dupont, A. F. Feil and S. R. Teixeira, Ta_2O_5 Nanotubes Obtained by Anodization: Effect of Thermal Treatment on the Photocatalytic Activity for Hydrogen Production, *J. Phys. Chem. C*, 2012, **116**, 14022–14030, DOI: 10.1021/jp303273q.

7 M. Yang, H. He, A. Liao, J. Huang, Y. Tang, J. Wang, G. Ke, F. Dong, L. Yang, L. Bian and Y. Zhou, Boosted Water Oxidation Activity and Kinetics on $BiVO_4$ Photoanodes with Multihigh-Index Crystal Facets, *Inorg. Chem.*, 2018, **57**, 15280–15288, DOI: 10.1021/acs.inorgchem.8b02570.

8 J. H. Kim and J. S. Lee, $BiVO_4$-Based Heterostructured Photocatalysts for Solar Water Splitting: A Review, *Energy Environ. Focus*, 2014, **3**, 339–353, DOI: 10.1166/eef.2014.1121.

9 A. K. M. F. U. Islam, M. N. H. Liton, H. M. T. Islam, M. A. Helal and M. Kamruzzaman, Mechanical and thermodynamical stability of $BiVO_4$ polymorphs using first-

principles study, *Chin. Phys. B*, 2017, **26**, 36301, DOI: 10.1088/1674-1056/26/3/036301.

10 M. N. H. Liton, M. Roknuzzaman, M. A. Helal, M. Kamruzzaman, A. K. M. F. U. Islam, K. Ostrikov and M. K. R. Khan, Electronic, mechanical, optical and photocatalytic properties of perovskite $RbSr_2Nb_3O_{10}$ compound, *J. Alloys Compd.*, 2021, **867**, 159077, DOI: 10.1016/j.jallcom.2021.159077.

11 A. Chakraborty, M. N. H. Liton, M. S. I. Sarker, M. M. Rahman and M. K. R. Khan, A comprehensive DFT evaluation of catalytic and optoelectronic properties of $BaTiO_3$ polymorphs, *Phys. B: Condens. Matter*, 2023, **648**, 414418, DOI: 10.1016/j.physb.2022.414418.

12 M. N. H. Liton, M. A. Helal, A. K. M. Farid Ul Islam, M. Kamruzzaman, M. S. I. Sarker and M. K. R. Khan, Anisotropic elastic, opto-electronic and photocatalytic properties of $BaTi_2O_5$: first-principles calculations, *Mater. Sci. Eng., B*, 2023, **296**, 116658, DOI: 10.1016/j.mseb.2023.116658.

13 M. Monira, M. A. Helal, M. N. H. Liton, M. Kamruzzaman and S. Kojima, Elastic, optoelectronic and photocatalytic properties of semiconducting $CsNbO_3$: first principles insights, *Sci. Rep.*, 2023, **13**, 10246, DOI: 10.1038/s41598-023-36875-x.

14 G. J. Snyder and E. S. Toberer, Complex thermoelectric materials, *Nat. Mater.*, 2008, **7**, 105–114, DOI: 10.1038/nmat2090.

15 M. N. H. Liton, A. K. M. F. U. Islam, M. S. I. Sarker, M. M. Rahman and M. K. R. Khan, Unlocking the mechanical, thermodynamic and thermoelectric properties of $NaSbS_2$: a DFT scheme, *Heliyon*, 2025, **11**(1), e41220, DOI: 10.1016/j.heliyon.2024.e41220.

16 A. K. M. F. Ul Islam, M. A. Helal, M. N. H. Liton, M. Kamruzzaman and H. M. T. Islam, First principles study of electronic structure dependent optical properties of oxychalcogenides BiOCuCh (Ch = S, Se, Te), *Indian J. Phys.*, 2017, **91**, 403–412, DOI: 10.1007/s12648-016-0928-4.

17 I. S. Khare, N. J. Szymanski, D. Gall and R. E. Irving, Electronic, optical, and thermoelectric properties of sodium pnictogen chalcogenides: a first principles study, *Comput. Mater. Sci.*, 2020, **183**, 109818, DOI: 10.1016/j.commatsci.2020.109818.

18 S. Park and B. Ryu, Hybrid-density functional theory study on the band structures of tetradymite-Bi_2Te_3, Sb_2Te_3, Bi_2Se_3, and Sb_2Se_3 thermoelectric materials, *J. Korean Phys. Soc.*, 2016, **69**, 1683–1687, DOI: 10.3938/jkps.69.1683.

19 M. A. Rehman, J. U. Rehman and M. B. Tahir, Density functional theory study of structural, electronic, optical, mechanical, and thermodynamic properties of halide double perovskites Cs_2AgBiX_6 (X = Cl, Br, I) for photovoltaic applications, *J. Phys. Chem. Solids*, 2023, **181**, 111443, DOI: 10.1016/j.jpcs.2023.111443.

20 P. Qin, S. Tanaka, S. Ito, N. Tetreault, K. Manabe, H. Nishino, M. K. Nazeeruddin and M. Grätzel, Inorganic hole conductor-based lead halide perovskite solar cells with 12.4% conversion efficiency, *Nat. Commun.*, 2014, **5**, 3834, DOI: 10.1038/ncomms4834.

21 S. A. Mir, A. Q. Seh and D. C. Gupta, New ferromagnetic half-metallic perovskites for spintronic applications: $BaMO_3$ (M = Mg and Ca), *RSC Adv.*, 2020, **10**, 36241–36252, DOI: 10.1039/D0RA06739C.

22 S. A. Khandy and D. C. Gupta, New isostructural halide double perovskites Cs_2GeNiX_6 (X = Cl, Br) for semiconductor spintronics and thermoelectric advancements, *J. Solid State Chem.*, 2021, **300**, 122196, DOI: 10.1016/j.jssc.2021.122196.

23 H. Abdy, A. Aletayeb, M. Bashirpour, Z. Heydari, M. Kolahdouz, E. Asl-Soleimani, Z. Kolahdouz and G. Zhang, Synthesis, optical characterization, and simulation of organo-metal halide perovskite materials, *Optik*, 2019, **191**, 100–108, DOI: 10.1016/j.ijleo.2019.06.007.

24 S. Berri and N. Bouarissa, Ab initio study of fundamental properties of $ACdX_3$ (A = K, Rb, Cs; and X = F, Cl, Br) halide perovskite compounds, *Emergent Mater.*, 2023, **6**, 1009–1025, DOI: 10.1007/s42247-023-00488-x.

25 H. Baaziz, T. Ghellab and Z. Charifi, Properties of the chalcogenide-based double perovskites Ba_2NbBiS_6 and Ba_2TaSbS_6 with respect to structural, electronic and optical aspects, *Int. J. Mod. Phys. B*, 2025, **39**, 2550066, DOI: 10.1142/S0217979225500663.

26 A. Zikem, H. Baaziz, T. Ghellab, Z. Charifi and F. Soyalp, Electronic, optical, and thermoelectric properties of vacancy-ordered double perovskite K_2SnX_6 (X = Cl, Br, I) from first-principle calculations, *Phys. Scr.*, 2024, **99**, 035917, DOI: 10.1088/1402-4896/ad1ad8.

27 T. Ghellab, H. Baaziz and Z. Charifi, Enhanced thermoelectric performance of double perovskites Ba_2NbBiS_6 and Ba_2TaSbS_6 via carrier engineering and chemical potential tuning, *Comput. Condens. Matter*, 2025, **44**, e01083, DOI: 10.1016/j.cocom.2025.e01083.

28 A. Alsaad, A. Telfah, H. Baaziz, T. Ghellab, Z. Charifi, S. Abdalla, W.-N. Mei and R. Sabirianov, Ab initio investigation of mechanical, electronic and optical properties in the orthorhombic $CsPbI_3$ inorganic perovskite, *Mater. Sci. Semicond. Process.*, 2024, **177**, 108375, DOI: 10.1016/j.mssp.2024.108375.

29 A. Siddique, A. Khalil, B. S. Almutairi, M. Bilal Tahir, T. Ahsan, A. Hannan, H. Elhosiny Ali, H. Alrobei and M. Alzaid, Structural, electronic, mechanical and dynamical stability properties of $LiAH_3$ (A = Sc, Ti & V) perovskite-type hydrides: a first principle study, *Chem. Phys.*, 2023, **568**, 111851, DOI: 10.1016/j.chemphys.2023.111851.

30 L. Abbes and H. Noura, Perovskite oxides $MRuO_3$ (M = Sr, Ca and Ba): structural distortion, electronic and magnetic properties with GGA and GGA-modified Becke–Johnson approaches, *Results Phys.*, 2015, **5**, 38–52, DOI: 10.1016/j.rinp.2014.10.004.

31 H. Arif, M. B. Tahir, B. S. Almutairi, I. Khalid, M. Sagir, H. Elhosiny Ali, H. Alrobei and M. Alzaid, CASTEP study for mapping phase stability, and optical parameters of halide perovskite $CsSiBr_3$ for photovoltaic and solar cell applications, *Inorg. Chem. Commun.*, 2023, **150**, 110474, DOI: 10.1016/j.inoche.2023.110474.

32 M. Sakata, T. Nishiwaki and J. Harada, Neutron Diffraction Study of the Structure of Cubic $CsPbBr_3$, *J. Phys. Soc. Jpn.*, 1979, **47**, 232–233, DOI: **10.1143/JPSJ.47.232**.

33 J. M. Leger, A. M. Redon, C. Andraud and F. Pelle, Isotropic compression of the linear-chain perovskite-type $CsCdBr_3$ up to 20 GPa, *Phys. Rev. B: Condens. Matter Mater. Phys.*, 1990, **41**, 9276–9282, DOI: **10.1103/PhysRevB.41.9276**.

34 G. Natta and L. Passerini, Isomorfismo, polimorfismo e morfotropia. – I. Composti del tipo ABX_3, *Gazz. Chim. Ital.*, 1928, **58**, 472–484.

35 C. K. Møller, H. Saarinen, E. Näsäkkälä, M. Pouchard, P. Hagenmuller and A. F. Andresen, About the Crystal Structure of Cesium Cadmium Tribromide and Some Observations on Crystals of Cesium Cadmium Trichloride, *Acta Chem. Scand.*, 1977, **31a**, 669–672, DOI: **10.3891/acta.chem.scand.31a-0669**.

36 D. N. Vtyurina, I. A. Kaurova, G. M. Kuz'micheva, V. B. Rybakov, D. Y. Chernyshov, E. V. Khramov, S. V. Firstov and V. N. Korchak, Structural peculiarities, point defects and luminescence in Bi-doped $CsCdX_3$ (X = Cl, Br) single crystals, *J. Alloys Compd.*, 2019, **803**, 912–921, DOI: **10.1016/j.jallcom.2019.06.308**.

37 J. Guo, Q. Hu, M. Lu, A. Li, X. Zhang, R. Sheng, P. Chen, Y. Zhang, J. Wu, Y. Fu, G. Sun, W. W. Yu and X. Bai, Pb^{2+} doped $CsCdBr_3$ perovskite nanorods for pure-blue light-emitting diodes, *Chem. Eng. J.*, 2022, **427**, 131010, DOI: **10.1016/j.cej.2021.131010**.

38 E. Virey, M. Couchaud, C. Faure, B. Ferrand, C. Wyon and C. Borel, Room temperature fluorescence of $CsCdBr_3$: Re (Re = Pr, Nd, Dy, Ho, Er, Tm) in the 3–5-μm range, *J. Alloys Compd.*, 1998, **275–277**, 311–314, DOI: **10.1016/S0925-8388(98)00329-6**.

39 R. B. Barthem, R. Buisson and R. L. Cone, Spectroscopic analysis of Nd^{3+} pairs in $CsCdBr_3$, *J. Chem. Phys.*, 1989, **91**, 627–632, DOI: **10.1063/1.457167**.

40 J. R. Quagliano, N. J. Cockroft, K. E. Gunde and F. S. Richardson, Optical characterization and electronic energy-level structure of Er^{3+}-doped $CsCdBr_3$, *J. Chem. Phys.*, 1996, **105**, 9812–9822, DOI: **10.1063/1.472850**.

41 N. Hayashi, T. Terashima and M. Takano, Oxygen-holes creating different electronic phases in Fe^{4+}-oxides: successful growth of single crystalline films of $SrFeO_3$ and related perovskites at low oxygen pressure, *J. Mater. Chem.*, 2001, **11**, 2235–2237, DOI: **10.1039/B103259N**.

42 C. N. R. Rao and K. J. Rao, *Phase Transition in Solids: An Approach to the Study of the Chemistry and Physics of Solids*, McGraw-Hill, New York, 1978.

43 M. Wenzel, M. Altwein, R. Demirbilek, B. Leu, J. Heber, J. Kübler, B. Bleeker and A. Meijerink, Band structure and excitons in $CsCdBr_3$, *J. Alloys Compd.*, 2000, **300–301**, 479–482, DOI: **10.1016/S0925-8388(99)00702-1**.

44 M. D. Segall, P. J. D. Lindan, M. J. Probert, C. J. Pickard, P. J. Hasnip, S. J. Clark and M. C. Payne, First-principles simulation: ideas, illustrations and the CASTEP code, *J. Phys.: Condens. Matter*, 2002, **14**, 2717, DOI: **10.1088/0953-8984/14/11/301**.

45 J. P. Perdew, K. Burke and M. Ernzerhof, Generalized Gradient Approximation Made Simple, *Phys. Rev. Lett.*, 1996, **77**, 3865–3868, DOI: **10.1103/PhysRevLett.77.3865**.

46 A. V. Krukau, O. A. Vydrov, A. F. Izmaylov and G. E. Scuseria, Influence of the exchange screening parameter on the performance of screened hybrid functionals, *J. Chem. Phys.*, 2006, **125**, 224106, DOI: **10.1063/1.2404663**.

47 D. Vanderbilt, Soft self-consistent pseudopotentials in a generalized eigenvalue formalism, *Phys. Rev. B: Condens. Matter Mater. Phys.*, 1990, **41**, 7892–7895, DOI: **10.1103/PhysRevB.41.7892**.

48 H. J. Monkhorst and J. D. Pack, Special points for Brillouin-zone integrations, *Phys. Rev. B: Condens. Matter Mater. Phys.*, 1976, **13**, 5188–5192, DOI: **10.1103/PhysRevB.13.5188**.

49 T. H. Fischer and J. Almlof, General methods for geometry and wave function optimization, *J. Phys. Chem.*, 1992, **96**, 9768–9774, DOI: **10.1021/j100203a036**.

50 S. J. Clark, M. D. Segall, C. J. Pickard, P. J. Hasnip, M. I. J. Probert, K. Refson and M. C. Payne, First principles methods using CASTEP, *Z. Kristallogr. – Cryst. Mater.*, 2005, **220**, 567–570, DOI: **10.1524/zkri.220.5.567.65075**.

51 B. Rameshe, R. Murugan and B. Palanivel, First principle study on electronic structure, structural phase stability, optical and vibrational properties of Ba_2ScMO_6 (M = Nb, Ta), *Int. J. Mod. Phys. B*, 2016, **30**, 1550246, DOI: **10.1142/S021797921550246X**.

52 M. N. H. Liton, M. A. Helal, M. K. R. Khan, M. Kamruzzaman and A. K. M. Farid Ul Islam, Mechanical and opto-electronic properties of α-$MoSi_2$: a DFT scheme with hydrostatic pressure, *Indian J. Phys.*, 2022, **96**, 4155–4172, DOI: **10.1007/s12648-022-02355-7**.

53 M. Grundmann, Kramers–Kronig Relations, in *The Physics of Semiconductors: An Introduction Including Nanophysics and Applications*, ed. M. Grundmann, Springer, Berlin, Heidelberg, 2010, pp. 775–776, DOI: **10.1007/978-3-642-13884-3_26**.

54 S. Saha, T. P. Sinha and A. Mookerjee, Electronic structure, chemical bonding, and optical properties of paraelectric $BaTiO_3$, *Phys. Rev. B: Condens. Matter Mater. Phys.*, 2000, **62**, 8828–8834, DOI: **10.1103/PhysRevB.62.8828**.

55 G. Murtaza, N. Yousaf, M. Yaseen, A. Laref and S. Azam, Systematic studies of the structural and optoelectronic characteristics of $CaZn_2X_2$ (X = N, P, As, Sb, Bi), *Mater. Res. Express*, 2018, **5**, 016304, DOI: **10.1088/2053-1591/aaa1c4**.

56 G. K. H. Madsen, J. Carrete and M. J. Verstraete, BoltzTraP2, a program for interpolating band structures and calculating semi-classical transport coefficients, *Comput. Phys. Commun.*, 2018, **231**, 140–145, DOI: **10.1016/j.cpc.2018.05.010**.

57 G. Kresse and J. Furthmüller, Efficient iterative schemes for ab initio total-energy calculations using a plane-wave basis set, *Phys. Rev. B: Condens. Matter Mater. Phys.*, 1996, **54**, 11169–11186, DOI: **10.1103/PhysRevB.54.11169**.

58 G. Kresse and J. Furthmüller, Efficiency of ab-initio total energy calculations for metals and semiconductors using a

plane-wave basis set, *Comput. Mater. Sci.*, 1996, **6**, 15–50, DOI: **10.1016/0927-0256(96)00008-0**.

59 T. Atsushi, First-principles Phonon Calculations with Phonopy and Phono3py, *J. Phys. Soc. Jpn.*, 2023, **92**, 012001, DOI: **10.7566/JPSJ.92.012001**.

60 A. Togo, L. Chaput, T. Tadano and I. Tanaka, Implementation strategies in phonopy and phono3py, *J. Phys.: Condens. Matter*, 2023, **35**, 353001, DOI: **10.1088/1361-648X/acd831**.

61 Md. S. Sorker, Md. R. Islam, A. Chakraborty and Md. A. Razzak Sarker, First-principles and experimental study to investigate structural, elastic, electronic, thermal, and optical properties of $KCdCl_3$ metal halide perovskite crystals, *AIP Adv.*, 2024, **14**, 045038, DOI: **10.1063/5.0206191**.

62 P. Ren, J. Qin, C. Chen and A. Novel Nonlinear, Optical Crystal for the IR Region: Noncentrosymmetrically Crystalline $CsCdBr_3$ and Its Properties, *Inorg. Chem.*, 2003, **42**, 8–10, DOI: **10.1021/ic025813y**.

63 A. Chakraborty, M. N. H. Liton, M. S. I. Sarker, M. M. Rahman and M. K. R. Khan, Exploration of the structural, vibrational, electronic, mechanical and thermal properties of $Ru_4Al_3B_2$ and $Ru_9Al_3B_8$: a DFT study, *RSC Adv.*, 2023, **13**, 28912–28930, DOI: **10.1039/D3RA05334B**.

64 R. Md, P. Islam and A. Mondal, Chakraborty, First-principles study of the ground-state properties of ternary borides with the Ru_3B_2X (X = Th, U) type structure: a comparative analysis, *Mater. Adv.*, 2025, **6**, 3293–3313, DOI: **10.1039/D5MA00091B**.

65 I. Ornelas-Cruz, R. M. dos Santos, J. E. González, M. P. Lima and J. L. F. D. Silva, Cubic-to-hexagonal structural phase transition in metal halide compounds: a DFT study, *J. Mater. Chem. A*, 2024, **12**, 12564–12580, DOI: **10.1039/D3TA06604E**.

66 A. Alaei, A. Circelli, Y. Yuan, Y. Yang and S. S. Lee, Polymorphism in metal halide perovskites, *Mater. Adv.*, 2021, **2**, 47–63, DOI: **10.1039/D0MA00643B**.

67 M. A. Fadla, B. Bentria, T. Dahame and A. Benghia, First-principles investigation on the stability and material properties of all-inorganic cesium lead iodide perovskites $CsPbI_3$ polymorphs, *Phys. B: Condens. Matter*, 2020, **585**, 412118, DOI: **10.1016/j.physb.2020.412118**.

68 I. A. Apon, S. Jubayer, R. Boudissa, R. Kawsar, R. Rafiu, M. S. Refat, Md. S. H. Saikot, A. M. Alsuhaibani, Md. A. Rahman, Md. A. Hossain and N. Elboughdiri, Exploring $ACdX_3$ Perovskites: DFT Analysis of Stability, Electronic, Optical, and Mechanical Properties for Solar Applications, *J. Inorg. Organomet. Polym. Mater.*, 2025, DOI: **10.1007/s10904-025-03821-5**.

69 R. I. Maphoto, M. T. Morukuladi, K. T. Malatji, M. C. Masedi and P. E. Ngoepe, First-Principle Study of $CsPbBr_3$ and $CsPbI_3$ Perovskite Solar Cells, *ECS J. Solid State Sci. Technol.*, 2022, **11**, 035012, DOI: **10.1149/2162-8777/ac5eb6**.

70 L. Huang and W. R. L. Lambrecht, Lattice dynamics in perovskite halides $CsSnX_3$ with X = I, Br, Cl, *Phys. Rev. B: Condens. Matter Mater. Phys.*, 2014, **90**, 195201, DOI: **10.1103/PhysRevB.90.195201**.

71 A. van Roekeghem, J. Carrete, C. Oses, S. Curtarolo and N. Mingo, High-Throughput Computation of Thermal Conductivity of High-Temperature Solid Phases: The Case of Oxide and Fluoride Perovskites, *Phys. Rev. X*, 2016, **6**, 041061, DOI: **10.1103/PhysRevX.6.041061**.

72 J. Yang, X. Wen, H. Xia, R. Sheng, Q. Ma, J. Kim, P. Tapping, T. Harada, T. W. Kee, F. Huang, Y.-B. Cheng, M. Green, A. Ho-Baillie, S. Huang, S. Shrestha, R. Patterson and G. Conibeer, Acoustic-optical phonon up-conversion and hot-phonon bottleneck in lead-halide perovskites, *Nat. Commun.*, 2017, **8**, 14120, DOI: **10.1038/ncomms14120**.

73 B. Holm, R. Ahuja, Y. Yourdshahyan, B. Johansson and B. I. Lundqvist, Elastic and optical properties of α- and κ-Al_2O_3, *Phys. Rev. B: Condens. Matter Mater. Phys.*, 1999, **59**, 12777–12787, DOI: **10.1103/PhysRevB.59.12777**.

74 T. K. Ghosh, M. N. H. Liton, A. Chakraborty, M. K. R. Khan and M. S. I. Sarker, Atomic position dependent structural, electronic, mechanical and optical properties of $ZnSbF_3$ fluoroperovskites, *Mater. Sci. Semicond. Process.*, 2025, **187**, 109065, DOI: **10.1016/j.mssp.2024.109065**.

75 X. Chen, S. Shen, L. Guo and S. S. Mao, Semiconductor-based Photocatalytic Hydrogen Generation, *Chem. Rev.*, 2010, **110**, 6503–6570, DOI: **10.1021/cr1001645**.

76 J. Liu, S. Chen, Q. Liu, Y. Zhu and J. Zhang, Correlation of crystal structures and electronic structures with visible light photocatalytic properties of $NaBiO_3$, *Chem. Phys. Lett.*, 2013, **572**, 101–105, DOI: **10.1016/j.cplett.2013.04.040**.

77 S. Berardi, S. Drouet, L. Francàs, C. Gimbert-Suriñach, M. Guttentag, C. Richmond, T. Stoll and A. Llobet, Molecular artificial photosynthesis, *Chem. Soc. Rev.*, 2014, **43**, 7501–7519, DOI: **10.1039/C3CS60405E**.

78 R. S. Mulliken, Electronic Population Analysis on LCAO–MO Molecular Wave Functions. II. Overlap Populations, Bond Orders, and Covalent Bond Energies, *J. Chem. Phys.*, 1955, **23**, 1841–1846, DOI: **10.1063/1.1740589**.

79 P. Pitriana, T. D. K. Wungu, Herman and R. Hidayat, The characteristics of band structures and crystal binding in all-inorganic perovskite $APbBr_3$ studied by the first principle calculations using the Density Functional Theory (DFT) method, *Results Phys.*, 2019, **15**, 102592, DOI: **10.1016/j.rinp.2019.102592**.

80 F. L. Hirshfeld, Bonded-atom fragments for describing molecular charge densities, *Theor. Chim. Acta*, 1977, **44**, 129–138, DOI: **10.1007/BF00549096**.

81 R. D. Harcourt, Diatomic antibonding σ^*s orbitals as "metallic orbitals" for electron conduction in alkali metals, *J. Phys. B: Atom. Mol. Phys.*, 1974, **7**, L41–L45, DOI: **10.1088/0022-3700/7/2/003**.

82 D. R. Solli, C. F. McCormick, C. Ropers, J. J. Morehead, R. Y. Chiao and J. M. Hickmann, Demonstration of Superluminal Effects in an Absorptionless, Nonreflective System, *Phys. Rev. Lett.*, 2003, **91**, 143906, DOI: **10.1103/PhysRevLett.91.143906**.

83 M. N. H. Liton, M. K. R. Khan and M. M. Rahman, Effect of N and Al-N dual doping on optical, photoluminescence and transport properties of ZnO films, *Mater. Res. Express*, 2015, **2**, 065903, DOI: **10.1088/2053-1591/2/6/065903**.

84 M. A. Haque Naeem, A. S. Rahman Ayon, Md. M. Ali, Md. R. Amin, M. H. Kabir, Md. A. Sattar, S. Tabassum and M. N. Huda Liton, Insights into the consequence of (Al–Zn) dual-doping on structural, morphological, and optoelectrical properties of CdO thin films, *Heliyon*, 2024, **10**, e26545, DOI: **10.1016/j.heliyon.2024.e26545**.

85 B. Gurunani and D. C. Gupta, Exploring the multifaceted properties: structural, electronic, magnetic, mechanical, thermodynamic, transport, and optical characteristics of rhodium-based half-Heusler alloys, *J. Mater. Sci.*, 2024, **59**, 12502–12525, DOI: **10.1007/s10853-024-09942-5**.

86 M. Born, On the stability of crystal lattices. I, *Math. Proc. Cambridge Philos. Soc.*, 1940, **36**, 160–172, DOI: **10.1017/S0305004100017138**.

87 Z. Ran, C. Zou, Z. Wei and H. Wang, VELAS: an open-source toolbox for visualization and analysis of elastic anisotropy, *Comput. Phys. Commun.*, 2023, **283**, 108540.

88 T. Krishnamoorthy, H. Ding, C. Yan, W. L. Leong, T. Baikie, Z. Zhang, M. Sherburne, S. Li, M. Asta, N. Mathews and S. G. Mhaisalkar, Lead-free germanium iodide perovskite materials for photovoltaic applications, *J. Mater. Chem. A*, 2015, **3**, 23829–23832, DOI: **10.1039/C5TA05741H**.

89 S. F. Pugh, Relations between the elastic moduli and the plastic properties of polycrystalline pure metals, *London, Edinburgh Dublin Philos. Mag. J. Sci.*, 1954, **45**, 823–843, DOI: **10.1080/14786440808520496**.

90 W. Feng and S. Cui, Mechanical and electronic properties of Ti_2AlN and Ti_4AlN_3: a first-principles study, *Can. J. Phys.*, 2014, **92**, 1652–1657, DOI: **10.1139/cjp-2013-0746**.

91 Y. Benaissa Cherif, M. Rouaighia, A. Zaoui and A. Boukortt, Optoelectronic, elastic and thermal properties of cubic perovskite-type $SrThO_3$, *Acta Phys. Pol., A*, 2017, **131**, 406–413, DOI: **10.12693/APhysPolA.131.406**.

92 Z. W. Huang, Y. H. Zhao, H. Hou and P. D. Han, Electronic structural, elastic properties and thermodynamics of $Mg_{17}Al_{12}$, Mg_2Si and Al_2Y phases from first-principles calculations, *Phys. B: Condens. Matter*, 2012, **407**, 1075–1081, DOI: **10.1016/j.physb.2011.12.132**.

93 M. E. Fine, L. D. Brown and H. L. Marcus, Elastic constants versus melting temperature in metals, *Scr. Metall.*, 1984, **18**, 951–956, DOI: **10.1016/0036-9748(84)90267-9**.

94 D. R. Clarke, Materials selection guidelines for low thermal conductivity thermal barrier coatings, *Surf. Coatings Technol.*, 2003, **163–164**, 67–74, DOI: **10.1016/S0257-8972(02)00593-5**.

95 Y. Liu, X. Zhao, Z. Yang, Z. Wang, X. Chen, S. Yang and M. Wei, New insights into element migration on $La_{0.6}Sr_{0.4}Co_{0.2}Fe_{0.8}O_{3-\delta}$ cathodes of intermediate temperature solid oxide fuel cells, *Solid State Ionics*, 2019, **334**, 145–151, DOI: **10.1016/j.ssi.2019.02.011**.

96 Y. Chen, X. L. Xu, G. H. Zhang, H. Xue and S. Y. Ma, Blue shift of optical bandgap in Er-doped ZnO thin films deposited by direct current reactive magnetron sputtering technique, *Phys. E*, 2010, **42**, 1713–1716, DOI: **10.1016/j.physe.2010.01.029**.

97 H. Niu, S. Niu and A. R. Oganov, Simple and accurate model of fracture toughness of solids, *J. Appl. Phys.*, 2019, **125**, 065105, DOI: **10.1063/1.5066311**.

98 H. Morkoç, *Handbook of Nitride Semiconductors and Devices: Electronic and Optical Processes in Nitrides*, Wiley, 1st edn, 2008, DOI: **10.1002/9783527628414**.

99 M. E. Levinshtein, S. L. Rumyantsev and M. S. Shur, *Properties of Advanced Semiconductor Materials: GaN, AIN, InN, BN, SiC, SiGe*, John Wiley & Sons, 2001.

100 R. O. Agbaoye, P. O. Adebambo and G. A. Adebayo, First principles comparative studies of thermoelectric and other properties in the cubic and hexagonal structure of $CsCdCl_3$ halide perovskites, *Comput. Condens. Matter*, 2019, **21**, e00388, DOI: **10.1016/j.cocom.2019.e00388**.

101 S. Saini, A. K. Baranwal, T. Yabuki, S. Hayase and K. Miyazaki, Growth of halide perovskites thin films for thermoelectric applications, *MRS Adv.*, 2019, **4**, 1719–1725, DOI: **10.1557/adv.2019.279**.

102 N. F. Mott, E. A. Davis, N. F. Mott and E. A. Davis, *Electronic Processes in Non-Crystalline Materials*, Oxford University Press, Oxford, New York, 2012.